

VCP functions to maintain nuclear size by managing DNA damage-induced MDC1–p53–autophagy axis

Ya-Chu Chang

National Tsing Hua University

Yu-Xiang Peng

National Tsing Hua University

Chao-Jie Shih

National Tsing Hua University

Henry Chang

Purdue University

Tzu-Kang Sang (✉ tkasang@life.nthu.edu.tw)

National Tsing Hua University

Article

Keywords: TER94, γ H2AV staining, nuclear morphology, DNA damage

Posted Date: August 12th, 2020

DOI: <https://doi.org/10.21203/rs.3.rs-49185/v1>

License:  This work is licensed under a Creative Commons Attribution 4.0 International License.

[Read Full License](#)

Version of Record: A version of this preprint was published at Nature Communications on July 12th, 2021. See the published version at <https://doi.org/10.1038/s41467-021-24556-0>.

1 **Title: VCP functions to maintain nuclear size by managing DNA damage-induced**
2 **MDC1–p53–autophagy axis**

3

4 Ya-Chu Chang^{1,3}, Yu-Xiang Peng¹, Chao-Jie Shih¹, Henry C. Chang², Tzu-Kang
5 Sang^{1,3*}

6 1 Institute of Biotechnology, Department of Life Science, National Tsing Hua University,
7 Hsinchu, Taiwan

8 2 Department of Biological Sciences, Purdue University, West Lafayette, Indiana,
9 United States of America

10 3 Brain Research Center, National Tsing Hua University, Hsinchu, Taiwan

11 * Corresponding author

12 Address: Institute of Biotechnology and Department of Life Science, National Tsing Hua
13 University, 101, Section 2, Kuang-Fu Road, Hsinchu 30013, Taiwan

14 Email: tksang@life.nthu.edu.tw

15 Phone: 886-3-5742474

16 FAX: 886-3-5715934

17

18

19

20

21

22

23

24

25

26

27

28

29

30

31

32

33

34 **Abstract**

35

36 Anomalies in nuclear morphology have been linked to aging-related diseases and
37 malignant transformation, although the mechanism responsible for this connection
38 remains unclear. By expressing dominant-negative TER94 (TER94^{K2A}) mutants in
39 *Drosophila* photoreceptors, we show disruption of VCP (valosin-containing protein,
40 TER94 ortholog in human), an AAA (ATPase associated with various cellular activities)
41 ATPase essential for ubiquitin-dependent segregation or degradation of proteins,
42 causes an age-dependent nuclear size increase. Loss of VCP function leads to
43 accumulations of MDC1 (mediator of DNA damage checkpoint protein 1), a key DNA
44 damage response gene, and increased γ H2AV (an indicator of DNA damage), linking
45 excessive DNA damages and associated responses to this enlarged nuclei defect.
46 Indeed, MDC1-overexpression, similar to TER94^{K2A}, increases γ H2AV staining and
47 nuclear size. Moreover, TER94 negatively influences MDC1 level and could interact
48 with MDC1, suggesting that MDC1 is a VCP substrate. MDC1 accumulation increases
49 p53 stability, and this VCP-MDC1-p53 connection is functional, as removal of p53
50 function suppresses the ability of TER94^{K2A} and MDC1 overexpression to increase
51 nuclear size. While p53 is capable of generating multiple isoforms, our genetic evidence
52 suggests that the p53A isoform specifically contributes to this TER94^{K2A}-associated
53 nuclear size increase. Combining our results with a previous report that p53A
54 expression disrupts autophagic flux, we propose that the failure of removing MDC1 in
55 TER94^{K2A}-expressing cells stabilizes p53A, which blocks autophagy and likely hinders
56 the removal of nuclear content, resulting in aberrant nuclear size increase.

57

58

59 Introduction

60

61 Aberrant nuclear morphology associates with aging¹ and serves as a pathological
62 hallmark in diseases like cancer and progeria^{2,3}. However, it is unclear whether the
63 change in nuclear size or shape has a direct role in causing aging/diseases or it
64 represents a byproduct of another cellular defect that causes aging/diseases. To
65 address this, it is critical to understand the processes that regulate nuclear morphology,
66 as well as the cellular stresses that alter nuclear shape. Accumulation of unrepaired
67 DNA damage is another common feature of the normal aging process in *Drosophila*, *C.*
68 *elegans*, and humans^{1,4,5}, implying a possible connection between nuclear morphology
69 and genome integrity in metazoan. Several types of malignant tumors show both
70 dysmorphic nuclei and disordered chromosomal arrangement^{2,6}. In this study, we use
71 *Drosophila* TER94 to decipher the molecular mechanisms linking nuclear morphological
72 change and DNA damage.

73 We have previously used *Drosophila* to model IBMPFD, a multi-system
74 degenerative disorder associated with specific mutations in VCP⁷. VCP ATPases form
75 hexamers and are known for extracting ubiquitinated proteins from organelles and
76 protein complexes for proteasome-mediated degradation, re-folding, or liberation⁸. VCP
77 has been implicated in numerous processes. In the cytoplasm, VCP responds to
78 stresses from the endoplasmic reticulum (ER) by participating in the ER-associated
79 degradation (ERAD) of misfolded ER proteins to maintain the homeostasis⁹. A similar
80 requirement for VCP function has also been reported for removing damaged proteins
81 during mitochondrial quality control¹⁰. VCP is essential for the maturation of
82 autophagosomes and their subsequent fusion with lysosomes^{11,12}. During mitotic
83 division, the nuclear envelope and Golgi reassembly also require VCP^{13,14}. In the
84 nucleus, this ubiquitin-dependent protein segregase/unfoldase has been reported to
85 remove or degrade several chromatin-associated proteins involved in DNA damage
86 response (DDR)¹⁵. With our *Drosophila* model, we show that IBMPFD alleles affect
87 energy consumption⁷. Whether *Drosophila* TER94 has a nuclear function is not clear.

88 Machinery repairing DNA lesions operates in a spatiotemporal-regulated precision,
89 completing the tasks of lesion sensing, signaling, and repairing. To achieve this, DDR

90 proteins recruited to the DNA damage sites for one task need to be displaced to allow
91 the assembly of complexes for a different task. This dynamic regulation involves several
92 post-translational modifications, including phosphorylation, ubiquitination, and SUMO
93 (small ubiquitin-like modifier)-conjugation¹⁶. For instance, in response to double-strand
94 breaks, the MRN (MRE11-RAD50-NBS1) sensor complex are loaded onto the damage
95 sites, facilitating the recruitment of phosphatidylinositol-3 kinase family protein ATM
96 (known as Tefu in fly) and ATM-dependent phosphorylation of the histone variant H2AX
97 (known as H2AV in fly)¹⁷. The phosphorylated H2AX (γ H2AX, known as γ H2AV in
98 *Drosophila*) then recruits MDC1 (known as Mu2 in fly), which serves as an adaptor for
99 additional factors to remodel chromatin near the DNA damage sites¹⁸. A SUMO-
100 targeted E3 ligase RNF4 (known as Dgrn in fly) mediates the ubiquitination of MDC1,
101 which promotes its subsequent dissociation from chromatin¹⁹. The removal of MDC1 is
102 required for the recruitment of downstream signaling and repair proteins, such as
103 53BP1 and BRCA1^{19,20}. However, how ubiquitin-conjugated MDC1 are removed from
104 chromatin is not understood.

105 In this study, we present evidence that loss of TER94 function leads to nuclear
106 size increase. Consistent with the known TER94 role, ubiquitinated proteins accumulate
107 inside the nucleus of TER94 dysfunction cells, and the extent of accumulation correlates
108 positively with the severity of this nuclear size defect. This TER94-associated nuclear
109 size defect is modified by Mu2 RNAi and overexpression, linking DDR to this process.
110 Genetic evidence further suggests the p53A isoform acts downstream of TER94 and
111 Mu2 in this aberrant nuclear size increase. TER94 interacts physically with Mu2 and
112 negatively regulates Mu2 level, suggesting Mu2 is a substrate of TER94. Mu2 positively
113 regulates p53 protein level, and is capable of directly interacting with p53. In addition,
114 TER94 dysfunction, in a Mu2- and p53-dependent manner, causes accumulation of
115 p62, a well-known indicator of disrupted autophagic flux. Together, our findings suggest
116 that TER94 dysfunction disrupts DDR, causing an accumulation of Mu2 proteins, which
117 stabilize p53 and perturb autophagy to enlarge the nuclei.

118

119 Results

120

121 Disruption of TER94 function causes nuclear enlargement in postmitotic cells

122 VCP is an essential gene, and whole-animal knockouts of VCP function in both fly and
123 mouse cause embryonic lethality^{21,22}. Thus, to analyze the cellular roles of VCP in
124 adults, we chose an alternative approach of expressing UAS-controlled dominant-
125 negative transgenes with tissue-specific GAL4 drivers. We have previously generated
126 UAS-TER94^{K2A} (K248A & K521A) and UAS-TER94^{E2Q} (E302Q & E575Q), which
127 overexpress *Drosophila* VCP mutants affecting ATP-binding and ATP-hydrolysis,
128 respectively^{23,24}. These variants with disabled ATPase activity are thought to act as
129 dominant-negatives by forming non-functional hexamers with endogenous wild type
130 TER94, thereby depleting the functional TER94 pool^{9,25}. When expressing TER94^{K2A}
131 with *Rh1*-GAL4 (hereafter referred as *Rh1*>TER94^{K2A}), a driver active in postmitotic
132 outer photoreceptor cells R1-R6 (R cells, Fig. 1a) from the late pupal stage on, we
133 observed an age-dependent increase in the nuclear size (Supplementary Fig. 1). As
134 revealed by anti-Lamin antibody staining, which labels the nuclear envelope, the R cell
135 nucleus transforms from a fringe-like shape (Supplementary Fig. 1a, 70% pupal) to a
136 round contour (Supplementary Fig. 1a, 0-day adult) at the pupae-to-adult transition. This
137 nuclear morphology transformation was similar in *Rh1*>*LacZ* control and
138 *Rh1*>TER94^{K2A}, indicating that expression of dominant-negative TER94 does not hinder
139 nuclear maturation during development. Instead, *Rh1*>TER94^{K2A} nuclei in 2-day-old
140 adults, compared to those of *Rh1*>*LacZ*, exhibited an apparent increase in nuclear size
141 (the *Rh1*>TER94^{K2A} nuclei were 35% larger than control; Supplementary Fig. 1). From
142 this point on, while *Rh1*>*LacZ* nuclear size remained constant, the *Rh1*>TER94^{K2A}
143 nuclei continued to enlarge, as they were 117% larger than the control in 5-day-old
144 adults (Fig. 1b, c and Supplementary Fig. 1), and 129% larger than the control in 8-day-
145 old adults (Supplementary Fig. 1). *Rh1*>TER94^{K2A} stained with anti-NPC (nuclear pore
146 complex) antibody yielded nuclear enlargement as well, indicating the abovementioned
147 phenotype was not caused by Lamin mis-localization (Fig. 1d). This expanded nuclear
148 size phenotype is specific, as the cell size revealed with a plasma membrane-
149 associated mCherry and rhabdomere size remained unaltered by TER94^{K2A} expression

150 (Supplementary Fig. 2). Together, these results showed that $TER94^{K2A}$ expression
151 causes a post-development and age-dependent nuclear size enlargement.

152 This expansion of nuclear size was not seen in cell overexpressing $TER94^{A229E}$
153 (Fig. 1b, c), an IBMPFD-associated variant, which we have previously shown to act as a
154 dominant-active mutant⁷. Overexpression of $TER94^{E2Q}$, a different dominant-negative
155 allele, also caused nuclear enlargement, indicating that this defect was not specific to
156 the $TER94^{K2A}$ variant (Fig. 1d). To further confirm that a loss of TER94 function causes
157 this nuclear size defect, we generated mosaic eyes containing mutant clones of
158 $TER94^{K15502}$ (a strong hypomorphic allele), and showed that homozygous $TER94^{K15502}$
159 cells, marked by the absence of GFP, exhibited enlarged nuclei as compared to the
160 neighboring normal cells (Fig. 1e). To ensure the nuclear size defect is not restricted to
161 the outer R cells, we used *Rh4-GAL4* driver, which is active in ~70% of R7 cells (Fig.
162 1a), to express *UAS-TER94^{K2A}* and *UAS-GFP-NLS* (*UAS-GFP-NLS* was included to
163 identify the $TER94^{K2A}$ -expressing R7 population). Consistent with the *Rh1>TER94^{K2A}*
164 results, R7 nuclei expressing $TER94^{K2A}$ (Fig. 1f, arrows) were larger than those without
165 $TER94^{K2A}$ expression (Fig. 1f, arrowheads). Expressing $TER94^{K2A}$ in other non-neuronal
166 postmitotic cells, such as cone cells and indirect flight muscle cells, recapitulated this
167 aberrant increase of nuclear size (Supplementary Fig. 3). Altogether, these data
168 suggest that TER94 AAA ATPase has a fundamental role in regulating nuclear size in
169 postmitotic cells, in which their nuclei are usually remained at a rather constant size.

170

171 **Loss of TER94 function causes accumulations of autophagic markers and** 172 **ubiquitinated nuclear proteins**

173 VCP hexamer is known to process ubiquitinated substrates for degradation in the
174 ubiquitin-proteasome system (UPS), and has been linked to autophagy, DDR, ERAD,
175 and apoptosis⁸. To determine whether disruption of any of the aforementioned
176 processes contributes to the nucleus expansion, we monitored the reporter activities for
177 these pathways in *Rh1>TER94^{K2A}* retina. In 2-day-old *Rh1>TER94^{K2A}* adults, while a
178 significant portion of nuclei were already enlarged, the activity of CD3 δ -YFP, an ERAD
179 reporter, remained low, implying that ERAD impairment is unlikely to be a cause
180 (Supplementary Fig. 4a). The signal of CD8-PARP-Venus, an apoptotic reporter, were

181 absent in 2-day-old *Rh1>TER94^{K2A}* adults and could only be detected in a few
182 *Rh1>TER94^{K2A}* cells one-week after the onset of nuclear expansion (Supplementary
183 Fig. 4b). Similarly, another independent apoptotic reporter, cleaved Caspase-3, was
184 appeared only in a subset of 5-day-old R7 cells expressing *TER94^{K2A}* by *Rh4-GAL4*
185 (Supplementary Fig. 4c). These observations preclude the notion of apoptosis being a
186 cause for enlarged nuclei.

187 To test whether *TER94^{K2A}* affects autophagy, we monitored the level of GFP-
188 Atg8a and GFP-p62 in *Rh1>TER94^{K2A}*. Atg8a is essential for autophagosome
189 formation²⁶ and p62 serves as an adaptor linking ubiquitinated substrates to Atg8²⁷. In
190 control retina, GFP-Atg8a and GFP-p62 signals were low and remained unchanged as
191 the flies aged (Fig. 2a, b). In contrast, both GFP-Atg8a and GFP-p62 showed age-
192 dependent increase in *Rh1>TER94^{K2A}* (Fig. 2a, b). Immunolabeling with anti-LC3 and
193 anti-ref(2)p respectively confirmed the accumulation of endogenous Atg8 and p62 in
194 *TER94* dysfunction cells (Supplementary Fig. 5). The GFP-Atg8a increase was both
195 cytoplasmic and nuclear, and correlated well with cells of large nuclei (Fig. 2a). While
196 the GFP-p62 increase also showed some correlation with cells of large nuclei, its
197 signals were more spatially restricted and age-dependent (Fig. 2b). Large GFP-p62
198 positive aggregates were seen primarily in the cytoplasm in 2-day-old retina, whereas
199 these structures were observed in both the cytoplasm and nuclei in 5-day-old retina
200 (Fig. 2a). Both autophagy GFP-tagged reporters were expressed from a heterologous
201 promoter (UAS), suggesting the observed increases are mediated by post-
202 transcriptional mechanisms. Furthermore, Atg8 and p62 are degraded after
203 autophagosome-lysosome fusion under normal condition, and a prolonged
204 accumulation of these two proteins has been associated with autophagy deregulation²⁸.
205 The fact that *Rh1>TER94^{K2A}* showed age-dependent accumulation of Atg8a and p62
206 suggests defective autophagy could be a contributing factor for the nuclear
207 enlargement.

208 To test whether disruption of *TER94* function affects the UPS system, we stained
209 *Rh1>TER94^{K2A}* adult retina with FK2, an antibody that recognizes mono- and
210 polyubiquitinated conjugates²⁹. At the late-pupal stage, at which the nuclear size of
211 *Rh1>TER94^{K2A}* outer R cells appeared normal, FK2 signal was seen in the nuclei of

212 only a few cells (Fig. 2c). As the flies aged, the FK2 signal intensity and number of cells
213 with nuclear FK2 staining increased, suggesting that *TER94^{K2A}* expression causes an
214 accumulation of ubiquitinated substrates. In comparison, no nuclear FK2 signal and only
215 occasional cytoplasmic FK2-positive puncta were detected in *Rh1>LacZ* (Fig. 2c). This
216 accumulation of ubiquitinated nuclear proteins was caused by loss of TER94 function,
217 confirmed by the FK2 immunostaining of mosaic tissues bearing homozygous
218 *TER94^{K15502}* clones (Fig. 2e). Importantly, the strength of FK2 signal correlated strongly
219 with the nuclear size increase (Fig. 2c, d). This correlation, along with the fact that the
220 appearance of FK2 staining precedes the enlarged nuclei defect, suggests the failure in
221 removing ubiquitinated nuclear proteins in *Rh1>TER94^{K2A}* cells is a cause for the
222 aberrant nuclear expansion.

223

224 **Disruption of nuclear TER94 function in DNA damage repair affects nuclear size**

225 VCP has known functions in both the cytoplasm and nucleoplasm⁸. Given the
226 correlation between ubiquitinated protein accumulation in the nucleus and the nuclear
227 size expansion, we speculated these defects were due to a deficit of TER94 function in
228 the nucleus. To test this hypothesis, we took advantage of a fortuitous finding of ours
229 that overexpression of Derlin-1, an ER membrane protein that recruits TER94 to the ER
230 vicinity upon ER stress, depletes the nuclear pool of endogenous TER94³⁰ (Fig. 3a, b).
231 Indeed, overexpression of Derlin-1 caused nuclear expansion (Fig. 3a, b), supporting
232 the notion that this nucleus enlargement was caused by a depletion of nuclear TER94.
233 As a control, expression of Derlin-1^{ΔSHP}, a Derlin-1 construct incapable of binding to
234 TER94³⁰, had no effect on the nuclear TER94 level and the nuclear size (Fig. 3a, b).
235 Furthermore, co-expression of wild type TER94 in *Rh1>Derlin-1* suppressed the nuclear
236 expansion phenotype (Supplementary Fig. 6), presumably by replenishing the level of
237 TER94 in the nucleus.

238 Within the nucleus, VCP function has been implicated in cell cycle and DDR
239 regulations^{31,32}. Using EdU incorporation assay, *Drosophila*-specific FUCCI
240 (Fluorescent Ubiquitination-based Cell Cycle Indicator) system (Fly-FUCCI)³³, and
241 another cell cycle reporter S/G2/M-Green, we showed that *Rh1>TER94^{K2A}* cells
242 remained mitotically inactive (Supplementary Fig. 7), indicating that the nuclear

243 morphological change is not caused by cell cycle re-entry. To test the impact of TER94
244 inactivation on DDR, we stained *Rh1>TER94^{K2A}* for γ H2AV, a phosphorylated histone
245 H2A variant formed at DNA damage sites to facilitate DDR processing^{34,35}. Like in
246 mammals, robust γ H2AV signals react to genotoxic insults in flies, as tested by H₂O₂
247 treatment (Fig. 3c). While this DDR marker signal remained unchanged in *Rh1>LacZ*
248 cells, γ H2AV staining increased in the nuclei of TER94^{K2A}-expressing cells (Fig. 3d, e).
249 More importantly, the elevation of γ H2AV staining in *Rh1>TER94^{K2A}* correlated with the
250 onset of nuclear size expansion. Like the nuclear enlargement phenotype, increased
251 γ H2AV staining was detected in homozygous *TER94^{K15502}* clones in mosaic eyes (Fig.
252 3f).

253 To independently confirm the effect of *Rh1>TER94^{K2A}* on DDR and to rule out the
254 possibility that *Rh1>TER94^{K2A}* merely altered H2AV expression, we tested another DDR
255 marker, PCNA (Proliferating Cell Nuclear Antigen), a DNA polymerase δ processivity
256 factor essential for both DNA replication and repair³⁶, and observed an elevation of
257 PCNA in *Rh1>TER94^{K2A}* (Fig. 3g). As we have excluded the possibility of
258 *Rh1>TER94^{K2A}* initiating DNA replication, this PCNA observation, along with the
259 abovementioned γ H2AV results, indicates that disruption of TER94 function perturbs the
260 DDR process, possibly causing an accumulation of unrepaired DNA lesions.

261

262 **Accumulation of *Drosophila* MDC1 phenocopies TER94^{K2A}-associated nuclear** 263 **enlargement**

264 The increase of DDR markers, as well as FK2 accumulation (Fig. 2), in *Rh1>TER94^{K2A}*
265 suggests that, in the absence of TER94 function, DDR proteins accumulated, leading to
266 enlarged nuclei. To test this hypothesis, we asked whether reduction of certain DDR
267 proteins, which might be TER94 substrates, could suppress the nucleus expansion
268 phenotype in *Rh1>TER94^{K2A}*. Conversely, if accumulation of certain DDR proteins is
269 responsible for the defect in *Rh1>TER94^{K2A}*, direct overexpression of these DDR
270 proteins should recapitulate the enlarged nuclei defect. Using these two criteria, we
271 screened DDR genes by RNA interference (RNAi) and *Rh1-GAL4*-driven
272 overexpression. RNAi-mediated knockdowns of several candidates, including *tefu*,
273 *l(3)mbt*, *mu2*, *bon*, *dgrn*, and *p53* (Fig. 4a and Supplementary Fig. 8a) showed

274 suppression of the nuclear enlargement defect, although only *Rh1>eGFP-mu2*, among
275 the tested constructs, presented a nuclear expansion phenotype similar to those seen in
276 *TER94^{K2A}* (Fig. 4b, c and Supplementary Fig. 8b). We made *UAS-mu2* transgenic flies
277 and showed *Rh1>mu2* photoreceptors contained enlarged nuclei (Fig. 5a), verifying that
278 this *mu2*-overexpression phenotype was unaffected by the GFP moiety. *Rh1>eGFP-*
279 *mu2*, similar to *Rh1>TER94^{K2A}*, showed increased γ H2AV staining (Fig. 4d, e),
280 consistent with our notion that accumulation of DDR proteins hinders DNA damage
281 repair. Moreover, the eGFP-Mu2 signal intensity in *Rh1>eGFP-mu2* correlated
282 positively with the nuclear size increase (Fig. 4f), strengthening our hypothesis that the
283 inability to remove Mu2 from the chromatin in *TER94^{K2A}* results in aberrant nuclear
284 morphology.

285 The similarities between *TER94^{K2A}* and Mu2-overexpression phenotypes suggest
286 these two genes act on the same pathway. Indeed, several lines of evidence suggest
287 that Mu2 is a substrate of TER94. Co-overexpression of wild type TER94 reduced
288 eGFP-Mu2 signals in the nuclei, and conversely, reduction of TER94 function by RNAi
289 increased nuclear eGFP-Mu2 signals (Fig. 4b, c, g). This influence of TER94 on Mu2
290 level was functional, as *TER94^{WT}* overexpression suppressed and *TER94* knockdown
291 enhanced Mu2-induced enlarged nuclei defect respectively (Fig. 4b, c). It is worth noting
292 that, as both TER94 and Mu2 were expressed from a heterologous promoter (from UAS
293 directed by *Rh1-GAL4*), this effect of TER94 on apparent Mu2 expression is unlikely to
294 be transcriptional. Indeed, RT-PCR showed the level of Mu2 transcripts was unaffected
295 in *TER94^{K2A}*-expressing cells (Fig. 4h). Nevertheless, Western blot of *TER94^{K2A}* lysates
296 showed an increase in the endogenous Mu2 (Fig. 4i), indicating that loss of TER94
297 function increased Mu2 protein level via a post-transcriptional mechanism. The *in situ*
298 proximity ligation assay (PLA) showed that TER94 interact with Mu2 *in vivo* (Fig. 4j).
299 The fact that TER94 regulates Mu2 abundance, along with this observation that these
300 two proteins are in close proximity, suggests that Mu2 is a potential TER94 substrate.

301

302 **p53A acts downstream of MDC1 in TER94 dysfunction-induced nuclear expansion**

303 To identify downstream effectors that contribute to this nuclear size increase, we looked
304 for proteins that are known to interact with Mu2 in literature and have significantly

305 modified the TER94^{K2A}-caused nuclear expansion in the abovementioned RNAi screen.
306 One such candidate is p53, which is known to interact with MDC1 in mammals^{37,38}. In
307 addition, RNAi-mediated downregulation of p53 suppressed both TER94^{K2A} and Mu2-
308 induced nuclear expansion (Fig. 4a and Fig. 5a). To independently confirm this role of
309 p53 in nuclear enlargement, we overexpressed TER94^{K2A} or Mu2 in homozygous p53
310 null (*p53*^{5A-1-4}; labeled as p53^{-/-})³⁹ background. Similar to the knockdown, a complete
311 removal of p53 function suppressed TER94^{K2A}- and Mu2-associated nuclear expansion
312 (Fig. 5b, c). These genetic interactions place p53 function downstream of TER94 and
313 Mu2 in this context.

314 The *Drosophila* p53 gene encodes four isoforms, A/C, B, D, and E (the isoform C
315 the same as isoform A), structurally differing by the length of the N-terminal
316 transactivation domain (TAD)⁴⁰. While the abovementioned genetic interactions link p53
317 to the TER94^{K2A}- associated nuclear size increase, it is unclear whether this particular
318 p53 role is isoform-specific. Quantitative Western analysis of *Rh1*>TER94^{K2A} adult
319 retinal extract detected no change in p53D and p53E level, a slight increase of p53B in
320 the nuclear fraction, and a significant increase of p53A in the cytosolic fraction (Fig. 5d).
321 To identify which p53 isoform(s) facilitates this TER94^{K2A}-dependent nuclear expansion,
322 we took advantage of the observation that p53^{-/-} suppressed the Mu2-associated
323 nuclear enlargement defect (see above). In *Rh1*>*eGFP-Mu2*; p53^{-/-} retina, expression of
324 p53B with *Rh1-GAL4* driver had no effect on the nuclear size (Fig. 5c), indicating that
325 this isoform has little, if any, role in this context. In contrast, expression of p53A in the
326 same background restored the nuclear size increase (Fig. 5c), strongly suggesting this
327 isoform contributes to the TER94^{K2A}-linked nuclear expansion phenotype.

328 In mammals, p53 proteins are labile⁴¹, and can be stabilized by MDC1 under
329 genotoxic stress⁴². p53 interacts with MDC1 directly through the BRCT (BRCA1 C-
330 terminal) domain^{37,38}, which is conserved in *Drosophila* Mu2⁴³. Thus it is reasonable to
331 hypothesize that Mu2 binds with and stabilizes p53 in affecting nuclear size. In support
332 of this, endogenous p53 was increased in *Rh1*>TER94^{K2A} (Fig. 5d), and exogenously
333 expressed p53A was elevated in tissues co-expressing TER94^{K2A} (Fig. 5e). Similarly,
334 ectopically expressed p53A was upregulated in Mu2-overexpression and reduced in
335 Mu2-RNAi backgrounds respectively (Fig. 5e). *In situ* PLA demonstrated that tagged

336 Mu2 could interact with p53A in eye discs (Fig. 5f). Taken together, these data support
337 a cascade, in which TER94^{K2A} increases Mu2 abundance to stabilize p53. In addition,
338 the stabilized p53 might be an effector mediating the nuclear expansion.

339

340 **TER94^{K2A} nuclear expansion is associated with p53-mediated autophagy flux**
341 **impairment**

342 Expression of *Drosophila* p53A in photoreceptors has been reported to impair
343 autophagic flux⁴⁴. As p53A contributes specifically to the nuclear enlargement defect
344 and TER94^{K2A} causes age-dependent Atg8a and p62 accumulation (Fig. 2a, b), we
345 hypothesized that TER94 dysfunction, in a Mu2- and p53-dependent manner, could
346 disrupt autophagic flux. Disrupted autophagic flux might fail to remove damaged nuclear
347 components, resulting in the observed nuclear size increase in *Rh1>TER94^{K2A}*. To
348 address this, we monitored the signal intensities of GFP-Atg8a or GFP-p62
349 in *Rh1>TER94^{K2A}* eyes co-expressing RNAi constructs against p53 or Mu2. Compared
350 to *Rh1>TER94^{K2A}* alone, knockdowns of p53 and Mu2 significantly reduced the GFP-
351 Atg8a and GFP-p62 signals (Fig. 6a-c), demonstrating that TER94^{K2A} causes
352 autophagy incompleteness through a Mu2- and p53-dependent manner.

353 To confirm the autophagy flux impairment and nuclear size enlargement are
354 facilitated by p53A, we compared the endogenous p62 levels and the nuclear sizes in R
355 cells expressing Mu2 alone with those co-expressing p53A. Compared to LacZ control,
356 Mu2 overexpression alone showed a slight but reproducible increase of p62. The p62
357 signal in *Rh1>Mu2* was strongly enhanced when p53A were co-expressed. Co-
358 expression of p53B showed little effect on p62 signal, demonstrating the specificity of
359 the enhancement by p53A (Fig. 6d). Likewise, the moderately enlarged nuclear size in
360 *Rh1>Mu2* expanded further with p53A co-expression (Fig. 6d). Together, these results
361 show that TER94^{K2A} and Mu2 overexpression cause autophagic flux defect and nuclear
362 enlargement through p53A.

363

364

365 **Discussion**

366

367 We have used *Drosophila* visual system to investigate the physiological function of VCP
368 and the mechanism by which specific VCP alleles contribute to neurodegeneration⁷.
369 Here, using both cell-specific expression of dominant-negative TER94 mutants and
370 FLP-induced *TER94*^{k15502} mutant clones, we show that removal of TER94 function in
371 postmitotic cells leads to an aberrant nuclear expansion. This enlarged nucleus
372 phenotype is not restricted to photoreceptors, as the expression of TER94^{K2A} in other
373 cell types generates a similar defect, suggesting that the role of TER94 in nuclear size
374 regulation is fundamental to most cells. Altered nuclear size or shape has been
375 associated with aging and diseases like cancer, although the mechanistic link between
376 aberrant nuclear morphology and cell pathophysiology is not well understood. While
377 multiple explanations likely exist for aberrant nuclear enlargement, the known roles of
378 VCP in degenerative disorders and the specificity of TER94^{K2A} nuclear enlargement
379 defect suggest this is an ideal model system to explore the underlying mechanism.

380 As the molecular function of VCP has been extensively studied, we suspect that
381 the enlarged nuclei defect may be linked to one of its characterized roles. We have
382 previously shown that overexpression of Derlin-1, a direct interactor of TER94, retains
383 TER94 in the cytoplasm³⁰. Derlin-1-dependent depletion of nuclear TER94 causes
384 enlarged nuclei, suggesting this nuclear enlargement is caused by disruption of TER94
385 function in the nucleus. In support of this, TER94^{K2A}-expressing R cells show elevated
386 levels of ubiquitinated proteins inside the nucleus, and the level of ubiquitination
387 correlates well with the severity of the nuclear size. Taken together, our results suggest
388 that the clearance of some ubiquitinated nuclear proteins is blocked by TER94^{K2A},
389 thereby causing nuclear enlargement.

390 VCP has been shown to rapidly accumulate at DNA damage site, facilitating the
391 extraction of chromatin-tethering proteins such as L3MBTL1 and KAP1 to assist the
392 recruitment of 53BP1 or BRCA1 respectively^{45,46}, and the removal of Ku80 from DNA at
393 the end of non-homologous end joining repair⁴⁷. Knockdowns of fly L3MBT and Ku80
394 suppress the *Rh1*>*TER94*^{K2A}-associated nuclear enlargement, linking DNA repair to this
395 aberrant nuclear morphology. This hypothesis is further supported by our analysis of

396 MDC1, a scaffold protein that bridges the injured DNA and DDR factors^{42,48,49}. Mu2, the
397 fly homolog of MDC1, modifies the phenotype of *Rh1>TER94^{K2A}*, and Mu2
398 overexpression recapitulates the phenotype of *Rh1>TER94^{K2A}*, placing Mu2
399 downstream of TER94 in this context. As TER94 is pleiotropic, this evidence of Mu2
400 overexpression phenocopies TER94^{K2A} supports that DDR participates specifically in
401 nuclear expansion. MDC1 is indispensable for DDR; however, prolonged retention of
402 MDC1 on DNA damage site impedes the access of downstream signaling or repairing
403 proteins^{19,20,50}. In support of the notion that a coordinated removal of MDC1- γ H2AX
404 association is critical for maintaining genomic stability, we observed persistent γ H2AV
405 signals in Mu2-overexpressing cells. The SUMO-targeted ubiquitin ligase RNF4 and the
406 deubiquitinase Ataxin-3 have been shown to regulate the removal of MDC1 from
407 chromatin⁵¹. Our demonstration that TER94 negatively influences Mu2 level via a post-
408 transcriptional manner suggests TER94 has a role in removing Mu2 as well. Combined
409 with the result of *in situ* PLA demonstrating that TER94 interacts with Mu2, Mu2 could
410 be a direct substrate of TER94. Thus, we propose that TER94-mediated degradation of
411 Mu2 is a crucial step permitting the DNA repair machinery to engage the lesion site.

412 During DDR, MDC1 serves as a binding platform for recruiting downstream DDR
413 factors^{42,48} including p53. Our observation that p53-RNAi suppresses both TER94^{K2A}
414 and Mu2-induced nucleus expansion places p53 downstream of these two proteins in
415 promoting nuclear size increase. The PLA assay confirms an interaction between Mu2
416 and p53. Furthermore, the Western blotting results show Mu2 overexpression boosts
417 p53 levels, suggesting that this Mu2-p53 interaction stabilizes labile p53 proteins. In
418 mammalian systems, p53 protein level under normal condition is kept low, as most of
419 p53 proteins are destined for degradation via a continuous ubiquitination by E3 ubiquitin
420 ligase MDM2. In the presence of DNA damage, phosphorylation of p53 by various
421 kinases could disturb this MDM2-p53 interaction and stabilize p53⁵². It has been
422 reported that MDC1 is indispensable for CHK2-mediated p53 phosphorylation and
423 stabilization in response to ionizing radiation in mammalian cells⁴². The observation that
424 Mu2 overexpression positively and Mu2-RNAi negatively regulates p53 protein level
425 respectively suggests a similar mechanism may exist in *Drosophila*. In support of this,
426 MDC1 is known to interact with p53 via the BRCT domain^{37,38}, which is conserved in

427 *Drosophila* Mu2⁴³. It is thought that the accumulated Mu2 represents a signal from
428 stalled DDR, and this Mu2-p53 interaction allows p53 to elicit responses to protect the
429 genome. Our demonstration that manipulating p53 level modifies nuclear size under
430 TER94^{K2A} or Mu2 overexpression suggests that alteration in nucleus structural
431 maintenance could be a response to stalled DDR.

432 The p53 locus is capable of generating multiple isoforms through the usage of
433 alternative promoters, splicing sites, and translational initiation sites⁵³. Our study
434 suggests the nuclear expansion defect, caused by TER94 dysfunction or Mu2-
435 overexpression, selectively requires p53A. Previous studies have suggested that p53A
436 is required for DNA damage-induced apoptosis in dividing cells by activating pro-
437 apoptotic genes⁴⁰, and this isoform also showed a tumor-suppressor function by
438 inducing apoptosis and necrosis during spermatogenesis⁵⁴. A recent report suggests
439 that *Drosophila* p53A and p53B have opposing effect on autophagy and apoptosis, and
440 it is the balance between these p53 isoforms that mediate this cellular life-and-death
441 decision under duress⁴⁴. Our observation that p53A is selectively required for this
442 context suggests that deregulated DDR, caused by either TER94 dysfunction or Mu2
443 accumulation, tips the balance to favor p53A-dependent response. In any case, our
444 work provides a new direction in resolving p53-regulated cellular events and
445 emphasizes the importance of unveiling factors controlling p53 abundance in an
446 isoform-specific fashion.

447 *Drosophila* p53A have recently been reported to disrupt autophagy flux⁴⁴. As our
448 analysis implicates p53A, it seems plausible that a disruption of autophagy has a role in
449 this TER94^{K2A}-associated enlarged nuclei defect. Indeed, TER94^{K2A} cells exhibit age-
450 dependent p62 accumulation, a well-established indicator of autophagy deficiency²⁸.
451 Furthermore, downregulation of Mu2 or p53 ameliorates the p62 accumulation in
452 *Rh1>TER94^{K2A}*, indicating that this autophagy deficiency is mediated by Mu2 and p53.
453 In addition to regulating chromatin modification⁵⁵, autophagy has been shown to remove
454 nuclear components upon genotoxic insults⁵⁶. Thus, p53A expression may disrupt
455 autophagy-mediated removal of nuclear components, thereby increasing the nuclear
456 size. Taken together, we propose a model (Fig. 6e) that VCP dysfunction causes
457 aberrant accumulation of MDC1 on the DNA damage foci. The MDC1 accumulation

458 then stabilizes p53A, which hinders the autophagy-dependent removal of nuclear
459 materials and alters the nuclear size.

460 Nearly 150 years ago, Sir Lionel Beale, the father of cytology, described different
461 nuclear morphology in various tumor types and recognized its prognostic value⁵⁷.

462 Nuclear morphometry, including changes in nuclear size or shape, and the presence of
463 nuclear lobulation, have since been extensively used to grade different tumors and
464 optimize clinical treatment. As altered VCP expression is also associated with poor
465 prognosis and sometimes linked to the metastatic potential in several cancer types⁵⁸⁻⁶³,
466 our study provides a plausible explanation of how VCP dysfunction, the nuclear
467 structure, and defective DDR could be linked. Furthermore, the identification of MDC1 is
468 a key player in stabilizing p53 during DDR, and by which to modulate autophagy and
469 nuclear morphology opens a new direction for the field studying p53-mediated cellular
470 responses. Our findings might help in developing new targets for clinical applications.

471

472 **Materials and Methods**

473

474 ***Drosophila* genetics and molecular biology**

475 Flies were raised on standard cornmeal food at 25°C under 12 hours light/dark
476 cycles unless otherwise mentioned. The following *Drosophila* strains were used: *Rh4-*
477 *GAL4*, *Spa-GAL4*, *Mhc-GAL4*, *UAS-tub-GAL80^{ts}*, *UAS-GFP-NLS*, *hs-FLP*, *FRT42D*
478 *GMR-myr.GFP*, *UAS-CD4-mCherry*, *UAS-EGFP.mu2*, Fly-FUCCI (*UAS-GFP-E2F1₁₋₂₃₀*,
479 *UAS-mRFP1-NLS-CycB₁₋₂₆₆*) (Bloomington *Drosophila* Stock Center, Indiana, USA),
480 *FRT42D TER94^{K15502}*, *UAS-S/G2/M-Green* (Kyoto Stock Center, Kyoto, Japan), *GMR-*
481 *GAL4* (originally derived from Dr. Matthew Freeman⁶⁴), *Rh1-GAL4* (provided by Dr.
482 Larry Zipursky), *UAS-CD8-PARP-Venus* (gift of Dr. Darren Williams), *UAS-GFP-Atg8a*
483 and *UAS-GFP-p62* (originally derived from Dr. Thomas Neufeld), *UAS-6XMyc-p53*
484 isoforms (kindly provided by Dr. Brian Calvi). All of the transgenic RNAi lines were
485 sourced from the *Drosophila* Stock Center (Bloomington, Indiana, USA) and the Vienna
486 *Drosophila* RNAi Center (Vienna, Austria). *UAS-CD3δ-YFP*, *UAS-TER94^{WT}*, *UAS-*
487 *TER94^{A229E}*, *UAS-TER94^{K2A}*, *UAS-TER94^{E2Q}*, *UAS-Derlin-1*, and *UAS-Derlin-1^{ΔSHP}* have
488 been previously described^{7,30}.

489 To generate somatic eye clones of *TER94^{K15502}*, *hs-FLP*; *FRT42D*, *GMR-myr.GFP*
490 virgins were crossed with *FRT42D*, *TER94^{K15502}/CyO* males. The F₁ progeny were
491 heat-shocked in a 37 °C water bath for 1 hour at second or third instar larval stage to
492 induce mitotic recombination. An additional 1-hour heat-shock a 37 °C on the following
493 day was administered to increase the frequency of recombination. Eye clones were
494 examined among F₁ adults without CyO.

495 To generate *pUAST-Mu2* construct, *Drosophila* Mu2 was excised from cDNA clone
496 LD44171 (*Drosophila* Genomics Resource Center, Indiana, USA) and subcloned into
497 *pUAST* as a KpnI-XbaI fragment. The *pUAST-Mu2* construct was verified by
498 sequencing prior to transgenic fly production by P element-mediated transformation⁶⁵
499 (WellGenetics, Taiwan).

500

501 **Antibody production and immunohistochemistry**

502 To generate polyclonal anti-TER94, anti-p53, and anti-Mu2 antibodies,
503 polypeptides corresponding to the amino acids 701-801 of TER94, amino acids 373-495
504 of p53, and the amino acids 627-947 of Mu2 respectively were bacterially expressed,
505 purified, and used for immunization (GeneTex). Whole-mount preparation of fly eyes
506 and eye discs were performed as previously described^{66,67}. Primary antibodies used
507 were the following: mouse anti-Lamin Dm0 (1:20, Developmental Studies Hybridoma
508 Bank, DSHB), rabbit anti-Lamin Dm0 (1:2,000, a generous gift from Dr. Paul Fisher),
509 rabbit anti-TER94 (1:500), mouse anti-Nuclear Pore Complex Proteins (NPC) (1:100,
510 Abcam), mouse anti- mono- and polyubiquitinated conjugates (FK2) (1:100, Enzo Life
511 Sciences), rabbit anti-ref(2)p (1:20, Abcam), rabbit anti-LC3A/B (1:20, Abcam), rabbit
512 anti-V5 (1:200, Millipore), mouse anti- γ H2Av (1:200, DSHB), mouse anti-PCNA (1:20,
513 Abcam), mouse anti-GFP (1:500, DSHB), mouse anti-Myc (1:100, GeneTex), mouse
514 anti-p53 (H1) (1:10, DSHB), rabbit anti-mCherry (1:100, GeneTex), rabbit anti-cleaved
515 PARP (1:50, Abcam), rabbit anti-cleaved Caspase 3 (1:20, Cell Signaling). Alexa Fluor®
516 488, Cy3, and Cy5 conjugated secondary antibodies (Jackson ImmunoResearch
517 Laboratories) were used at 1:100 dilutions. F-Actin enriched rhabdomere was labeled
518 by Rhodamine-conjugated phalloidin (Sigma-Aldrich). Zeiss LSM-510 or 800 confocal
519 microscopes were used for collecting all fluorescent images. Photoshop CS was used
520 for image processing. For experiments that comparing fluorescent-labeled probes
521 among different genotypes, the sample preparation and image processing was
522 performed with the same procedure and setting.

523

524 **Quantification of the nuclear size**

525 The nuclear and the rhabdomeral area are manually outlined according to the
526 Lamin and phalloidin staining respectively and measured by Image J. The area of each
527 nucleus is normalized to the area of its corresponding rhabdomere.

528

529 **Subcellular fractionation**

530 Subcellular fractionations to isolate nuclear and cytosolic proteins were performed
531 as described by Nabbi and Riabowol⁶⁸ with modifications. Briefly, fly heads of
532 appropriate genotypes were homogenized in ice-cold PBS containing 0.1% NP-40

533 supplemented with protease inhibitor cocktail (Roche). While 25% of the homogenates
534 (the whole cell lysates) were saved on ice, the remaining homogenates were
535 centrifuged for 30 sec at 10,000 rpm. The resulting supernatant (the cytosolic fraction)
536 was kept on ice, whereas the pellet was resuspended in ice-cold PBS containing 0.1%
537 NP-40 with protease inhibitor cocktail. The resuspended pellet was re-centrifuged for 30
538 sec at 10,000 rpm and the resulting pellet was resuspended in ice-cold PBS containing
539 0.1% NP-40 with protease inhibitor cocktail (the nuclear fraction). The whole cell lysates
540 and the nuclear fraction were sonicated on ice with two 8-sec pulses at 20 kHz, followed
541 by a centrifugation for 1 min at 13,200 rpm to remove the debris. The final whole cell
542 lysates and the nuclear fractions were obtained by collecting the supernatants after
543 centrifugation.

544

545 **Immunoblotting**

546 For Westerns, primary antibodies were used as the following dilutions: rabbit anti-
547 TER94 (1:5,000), rabbit anti-Histone H3 (1:40,000, Abcam), mouse anti- β -actin
548 (1:20,000, GeneTex), rabbit anti-GFP (1:1,000, GeneTex), rabbit anti-Mu2 (1:1,000),
549 and rabbit anti-p53 (1:500). Secondary antibodies conjugated with HRP (Jackson
550 ImmunoResearch Laboratories) were used in 1:10,000 dilutions. All loading controls
551 were prepared by stripping off the reagents from the original membrane and then re-
552 immunoblotting with anti- β -actin (for whole cell lysate and cytosolic fraction) or anti-
553 Histone H3 (for nuclear fraction) following the standard procedures.

554

555 **RT-PCR**

556 The total RNA from fly heads of *Rh1>LacZ*, *Rh1>TER94^{K2A}*, *Rh1>eGFP-Mu2* were
557 isolated using GENEzol™ TriRNA Pure Kit (Geneaid) following the manufacturer's
558 instructions. 4 μ g RNA was used for reverse transcription (Super-Script II, Invitrogen)
559 following the manufacturer's instructions. Subsequent PCR amplification was performed
560 with about 1 μ g cDNA. Specific primer pairs for TER94, Mu2, and internal control rp49
561 were listed in Table 1.

562

563 ***In situ* protein-protein interaction detection**

564 The Duolink[®] Proximity Ligation Assay (PLA) (Sigma-Aldrich) fluorescence method
565 was applied to detect *in situ* protein-protein interaction following the manufacturer's
566 instructions. Third instar larval eye discs expressing proteins of interests were used in
567 this assay. Rabbit anti-V5 (1:1,000, Millipore) and mouse anti-GFP (1:500, DSHB)
568 antibodies were used to assess interactions between TER94 and Mu2. Rabbit anti-Myc
569 (1:1,000, GeneTex) and mouse anti-GFP (1:500, DSHB) antibodies were used to
570 assess interactions between p53 and Mu2. Images were acquired with a Zeiss LSM 800
571 confocal microscope.

572

573 **EdU incorporation assay**

574 To determine whether cells re-entry cell cycle, Click-iT[®] EdU (Invitrogen) was used
575 following the manufacturer's instructions. Larval or adult retinas were dissected in PBS
576 and then incubated in S2 medium only (control) or S2 medium with 20 μ M EdU for 1.5
577 hours. After incubation, the tissues were fixed with 4% paraformaldehyde in PBS and
578 permeabilized with 0.5% Triton[®] X-100. Mouse anti-Lamin (1:20, DSHB) antibody was
579 used to label the nucleus. Zeiss LSM-510 confocal microscope was used for collecting
580 the images.

581

582

583

584 **References**

- 585 1 Scaffidi, P. & Misteli, T. Lamin A-dependent nuclear defects in human aging. *Science*
586 **312**, 1059-1063 (2006).
- 587 2 Uhler, C. & Shivashankar, G. V. Nuclear Mechanopathology and Cancer Diagnosis.
588 *Trends Cancer* **4**, 320-331, doi:10.1016/j.trecan.2018.02.009 (2018).
- 589 3 Goldman, R. D. *et al.* Accumulation of mutant lamin A causes progressive changes in
590 nuclear architecture in Hutchinson-Gilford progeria syndrome. *Proc Natl Acad Sci U S A*
591 **101**, 8963-8968, doi:10.1073/pnas.0402943101 (2004).
- 592 4 Haithcock, E. *et al.* Age-related changes of nuclear architecture in *Caenorhabditis*
593 *elegans*. *Proc Natl Acad Sci U S A* **102**, 16690-16695, doi:10.1073/pnas.0506955102
594 (2005).
- 595 5 Brandt, A., Krohne, G. & Grosshans, J. The farnesylated nuclear proteins KUGELKERN
596 and LAMIN B promote aging-like phenotypes in *Drosophila* flies. *Aging Cell* **7**, 541-551
597 (2008).
- 598 6 Zink, D., Fischer, A. H. & Nickerson, J. A. Nuclear structure in cancer cells. *Nat Rev*
599 *Cancer* **4**, 677-687 (2004).
- 600 7 Chang, Y. C. *et al.* Pathogenic VCP/TER94 alleles are dominant actives and contribute
601 to neurodegeneration by altering cellular ATP level in a *Drosophila* IBMPFD model.
602 *PLoS Genet* **7**, e1001288, doi:10.1371/journal.pgen.1001288 (2011).
- 603 8 Meyer, H., Bug, M. & Bremer, S. Emerging functions of the VCP/p97 AAA-ATPase in the
604 ubiquitin system. *Nat Cell Biol* **14**, 117-123, doi:10.1038/ncb2407 (2012).
- 605 9 Ye, Y., Meyer, H. H. & Rapoport, T. A. The AAA ATPase Cdc48/p97 and its partners
606 transport proteins from the ER into the cytosol. *Nature* **414**, 652-656 (2001).
- 607 10 Heo, J. M. *et al.* A stress-responsive system for mitochondrial protein degradation. *Mol*
608 *Cell* **40**, 465-480, doi:10.1016/j.molcel.2010.10.021 (2010).
- 609 11 Krick, R. *et al.* Cdc48/p97 and Shp1/p47 regulate autophagosome biogenesis in concert
610 with ubiquitin-like Atg8. *J Cell Biol* **190**, 965-973, doi:10.1083/jcb.201002075 (2010).
- 611 12 Ju, J. S. *et al.* Valosin-containing protein (VCP) is required for autophagy and is
612 disrupted in VCP disease. *J Cell Biol* **187**, 875-888, doi:10.1083/jcb.200908115 (2009).
- 613 13 Hetzer, M. *et al.* Distinct AAA-ATPase p97 complexes function in discrete steps of
614 nuclear assembly. *Nat Cell Biol* **3**, 1086-1091 (2001).
- 615 14 Rabouille, C. *et al.* Syntaxin 5 is a common component of the NSF- and p97-mediated
616 reassembly pathways of Golgi cisternae from mitotic Golgi fragments in vitro. *Cell* **92**,
617 603-610 (1998).
- 618 15 Torrecilla, I., Oehler, J. & Ramadan, K. The role of ubiquitin-dependent segregase p97
619 (VCP or Cdc48) in chromatin dynamics after DNA double strand breaks. *Philos Trans R*
620 *Soc Lond B Biol Sci* **372**, doi:10.1098/rstb.2016.0282 (2017).
- 621 16 Polo, S. E. & Jackson, S. P. Dynamics of DNA damage response proteins at DNA
622 breaks: a focus on protein modifications. *Genes Dev* **25**, 409-433,
623 doi:10.1101/gad.2021311 (2011).
- 624 17 Panier, S. & Durocher, D. Push back to respond better: regulatory inhibition of the DNA
625 double-strand break response. *Nat Rev Mol Cell Biol* **14**, 661-672, doi:10.1038/nrm3659
626 (2013).
- 627 18 Huen, M. S. *et al.* RNF8 transduces the DNA-damage signal via histone ubiquitylation
628 and checkpoint protein assembly. *Cell* **131**, 901-914, doi:10.1016/j.cell.2007.09.041
629 (2007).
- 630 19 Galanty, Y., Belotserkovskaya, R., Coates, J. & Jackson, S. P. RNF4, a SUMO-targeted
631 ubiquitin E3 ligase, promotes DNA double-strand break repair. *Genes Dev* **26**, 1179-
632 1195, doi:10.1101/gad.188284.112 (2012).

633 20 Shi, W. *et al.* Disassembly of MDC1 foci is controlled by ubiquitin-proteasome-
634 dependent degradation. *J Biol Chem* **283**, 31608-31616, doi:10.1074/jbc.M801082200
635 (2008).

636 21 Müller, J. M., Deinhardt, K., Rosewell, I., Warren, G. & Shima, D. T. Targeted deletion of
637 p97 (VCP/CDC48) in mouse results in early embryonic lethality. *Biochem Biophys Res*
638 *Commun* **354**, 459-465 (2007).

639 22 Ruden, D. M. *et al.* Membrane fusion proteins are required for oskar mRNA localization
640 in the Drosophila egg chamber. *Dev Biol* **218**, 314-325, doi:10.1006/dbio.1999.9583
641 (2000).

642 23 DeLaBarre, B., Christianson, J. C., Kopito, R. R. & Brunger, A. T. Central pore residues
643 mediate the p97/VCP activity required for ERAD. *Mol Cell* **22**, 451-462,
644 doi:10.1016/j.molcel.2006.03.036 (2006).

645 24 Mori-Konya, C. *et al.* p97/valosin-containing protein (VCP) is highly modulated by
646 phosphorylation and acetylation. *Genes Cells* **14**, 483-497, doi:10.1111/j.1365-
647 2443.2009.01286.x (2009).

648 25 Ye, Y., Meyer, H. H. & Rapoport, T. A. Function of the p97-Ufd1-Npl4 complex in
649 retrotranslocation from the ER to the cytosol: dual recognition of nonubiquitinated
650 polypeptide segments and polyubiquitin chains. *J Cell Biol* **162**, 71-84,
651 doi:10.1083/jcb.200302169 (2003).

652 26 Shpilka, T., Weidberg, H., Pietrokovski, S. & Elazar, Z. Atg8: an autophagy-related
653 ubiquitin-like protein. *Genome Biology* **12** (2011).

654 27 Mauvezin, C., Ayala, C., Braden, C. R., Kim, J. & Neufeld, T. P. Assays to monitor
655 autophagy in Drosophila. *Methods* **68**, 134-139, doi:10.1016/j.ymeth.2014.03.014
656 (2014).

657 28 Yoshii, S. R. & Mizushima, N. Monitoring and Measuring Autophagy. *Int J Mol Sci* **18**,
658 doi:10.3390/ijms18091865 (2017).

659 29 Fujimuro, M., Sawada, H. & Yokosawa, H. Production and characterization of
660 monoclonal antibodies specific to multi-ubiquitin chains of polyubiquitinated proteins.
661 *FEBS letters* **349**, 173-180 (1994).

662 30 Liang, C. J. *et al.* Derlin-1 regulates mutant VCP-linked pathogenesis and endoplasmic
663 reticulum stress-induced apoptosis. *PLoS Genet* **10**, e1004675,
664 doi:10.1371/journal.pgen.1004675 (2014).

665 31 Franz, A., Ackermann, L. & Hoppe, T. Ring of Change: CDC48/p97 Drives Protein
666 Dynamics at Chromatin. *Front Genet* **7**, 73, doi:10.3389/fgene.2016.00073 (2016).

667 32 Yamanaka, K., Sasagawa, Y. & Ogura, T. Recent advances in p97/VCP/Cdc48 cellular
668 functions. *Biochimica et biophysica acta* **1823**, 130-137,
669 doi:10.1016/j.bbamcr.2011.07.001 (2012).

670 33 Zielke, N. *et al.* Fly-FUCCI: A versatile tool for studying cell proliferation in complex
671 tissues. *Cell Rep* **7**, 588-598, doi:10.1016/j.celrep.2014.03.020 (2014).

672 34 Lake, C. M., Holsclaw, J. K., Bellendir, S. P., Sekelsky, J. & Hawley, R. S. The
673 development of a monoclonal antibody recognizing the Drosophila melanogaster
674 phosphorylated histone H2A variant (gamma-H2AV). *G3 (Bethesda)* **3**, 1539-1543,
675 doi:10.1534/g3.113.006833 (2013).

676 35 Mah, L. J., El-Osta, A. & Karagiannis, T. C. gammaH2AX: a sensitive molecular marker
677 of DNA damage and repair. *Leukemia* **24**, 679-686, doi:10.1038/leu.2010.6 (2010).

678 36 Essers, J. *et al.* Nuclear dynamics of PCNA in DNA replication and repair. *Mol Cell Biol*
679 **25**, 9350-9359, doi:10.1128/MCB.25.21.9350-9359.2005 (2005).

680 37 Nakanishi, M. *et al.* NFBD1/MDC1 Associates with p53 and Regulates Its Function at the
681 Crossroad between Cell Survival and Death in Response to DNA Damage. *J Biol Chem*
682 **282**, 22993-23004, doi:10.1074/jbc.M611412200 (2007).

683 38 Shahar, O. D. *et al.* Acetylation of lysine 382 and phosphorylation of serine 392 in p53
684 modulate the interaction between p53 and MDC1 in vitro. *PLoS One* **8**, e78472,
685 doi:10.1371/journal.pone.0078472 (2013).

686 39 Rong, Y. S. *et al.* Targeted mutagenesis by homologous recombination in *D.*
687 *melanogaster*. *Genes Dev* **16**, 1568-1581, doi:10.1101/gad.986602 (2002).

688 40 Zhang, B., Rotelli, M., Dixon, M. & Calvi, B. R. The function of *Drosophila* p53 isoforms
689 in apoptosis. *Cell Death Differ* **22**, 2058-2067, doi:10.1038/cdd.2015.40 (2015).

690 41 Giaccia, A. J. & Kastan, M. B. The complexity of p53 modulation: emerging patterns from
691 divergent signals. *Genes Dev* **12**, 2973-2983, doi:10.1101/gad.12.19.2973. (1998).

692 42 Lou, Z., Minter-Dykhouse, K., Wu, X. & Chen, J. MDC1 is coupled to activated CHK2 in
693 mammalian DNA damage response pathways. *NATURE* **421** (2003).

694 43 Dronamraju, R. & Mason, J. M. Recognition of double strand breaks by a mutator protein
695 (MU2) in *Drosophila melanogaster*. *PLoS Genet* **5**, e1000473,
696 doi:10.1371/journal.pgen.1000473 (2009).

697 44 Robin, M. *et al.* *Drosophila* p53 integrates the antagonism between autophagy and
698 apoptosis in response to stress. *Autophagy* **15**, 771-784,
699 doi:10.1080/15548627.2018.1558001 (2019).

700 45 Acs, K. *et al.* The AAA-ATPase VCP/p97 promotes 53BP1 recruitment by removing
701 L3MBTL1 from DNA double-strand breaks. *Nat Struct Mol Biol* **18**, 1345-1350,
702 doi:10.1038/nsmb.2188 (2011).

703 46 Kuo, C. Y., Li, X., Stark, J. M., Shih, H. M. & Ann, D. K. RNF4 regulates DNA double-
704 strand break repair in a cell cycle-dependent manner. *Cell Cycle* **15**, 787-798,
705 doi:10.1080/15384101.2016.1138184 (2016).

706 47 van den Boom, J. *et al.* VCP/p97 Extracts Sterically Trapped Ku70/80 Rings from DNA
707 in Double-Strand Break Repair. *Mol Cell* **64**, 189-198, doi:10.1016/j.molcel.2016.08.037
708 (2016).

709 48 Coster, G. & Goldberg, M. The cellular response to DNA damage: A focus on MDC1 and
710 its interacting proteins. *Nucleus* **1**, 166-178, doi:10.4161/nucl.1.2.11176. Epub 2009 Dec
711 29 (2010).

712 49 Zhang, J., Ma, Z., Treszezamsky, A. & Powell, S. N. MDC1 interacts with Rad51 and
713 facilitates homologous recombination. *Nat Struct Mol Biol* **12**, 902-909,
714 doi:10.1038/nsmb991 (2005).

715 50 Luo, K., Zhang, H., Wang, L., Yuan, J. & Lou, Z. Sumoylation of MDC1 is important for
716 proper DNA damage response. *The EMBO journal* **31**, 3008-3019,
717 doi:10.1038/emboj.2012.158 (2012).

718 51 Pfeiffer, A. *et al.* Ataxin-3 consolidates the MDC1-dependent DNA double-strand break
719 response by counteracting the SUMO-targeted ubiquitin ligase RNF4. *The EMBO journal*
720 **36**, 1066-1083, doi:10.15252/emboj.201695151 (2017).

721 52 Kruse, J. P. & Gu, W. Modes of p53 regulation. *Cell* **137**, 609-622,
722 doi:10.1016/j.cell.2009.04.050 (2009).

723 53 Marcel, V. *et al.* Biological functions of p53 isoforms through evolution: lessons from
724 animal and cellular models. *Cell Death Differ* **18**, 1815-1824, doi:10.1038/cdd.2011.120
725 (2011).

726 54 Napoletano, F. *et al.* p53-dependent programmed necrosis controls germ cell
727 homeostasis during spermatogenesis. *PLoS Genet* **13**, e1007024,
728 doi:10.1371/journal.pgen.1007024 (2017).

729 55 Wang, Y. *et al.* Autophagy Regulates Chromatin Ubiquitination in DNA Damage
730 Response through Elimination of SQSTM1/p62. *Mol Cell* **63**, 34-48,
731 doi:10.1016/j.molcel.2016.05.027 (2016).

732 56 Dou, Z. *et al.* Autophagy mediates degradation of nuclear lamina. *Nature* **527**, 105-109,
733 doi:10.1038/nature15548 (2015).

734 57 Koss, L. G. & Melamed, M. R. Koss' diagnostic cytology and its histopathologic bases
735 (Lippincott Williams & Wilkins, Philadelphia) 5th Ed. (2006).

736 58 Yamamoto, S. *et al.* Expression level of valosin-containing protein (p97) is correlated
737 with progression and prognosis of non-small-cell lung carcinoma. *Ann Surg Oncol* **11**
738 (2004).

739 59 Yamamoto, S. *et al.* Increased expression of valosin-containing protein (p97) is
740 associated with lymph node metastasis and prognosis of pancreatic ductal
741 adenocarcinoma. *Ann Surg Oncol* **11** (2004).

742 60 Yamamoto, S. *et al.* Expression of Valosin-Containing Protein in Colorectal Carcinomas
743 as a Predictor for Disease Recurrence and Prognosis. *Clin Cancer Res* **10** (2004).

744 61 Yamamoto, S. *et al.* Expression level of valosin-containing protein (VCP) as a prognostic
745 marker for gingival squamous cell carcinoma. *Ann Oncol* **15**, 1432-1438,
746 doi:10.1093/annonc/mdh354 (2004).

747 62 Yamamoto, S. *et al.* Elevated expression of valosin-containing protein (p97) in
748 hepatocellular carcinoma is correlated with increased incidence of tumor recurrence. *J*
749 *Clin Oncol* **21**, 447-452 (2003).

750 63 Tsujimoto, Y. *et al.* Elevated Expression of Valosin-Containing Protein (p97) Is
751 Associated with Poor Prognosis of Prostate Cancer. *Clin Cancer Res* **10**, 3007-3012
752 (2004).

753 64 Freeman, M. Reiterative Use of the EGF Receptor Triggers Differentiation of All Cell
754 Types in the Drosophila Eye. *Cell* **87**, 651-660 (1996).

755 65 Rubin, G. M. & Spradling, A. C. Genetic transformation of Drosophila with transposable
756 element vectors. *Science* **218**, 348-353 (1982).

757 66 Fan, S. S. & Ready, D. F. Glued participates in distinct microtubule-based activities in
758 Drosophila eye development. *Development* **124**, 1497-1507 (1997).

759 67 Sang, T. K. & Ready, D. F. Eyes closed, a Drosophila p47 homolog, is essential for
760 photoreceptor morphogenesis. *Development* **129**, 143-154 (2002).

761 68 Nabbi, A. & Riabowol, K. Rapid Isolation of Nuclei from Cells In Vitro. *Cold Spring Harb*
762 *Protoc* **2015**, 769-772, doi:10.1101/pdb.prot083733 (2015).

763

764

765

766

767

768

769

770

771

772

773 **Acknowledgements**

774 We like to thank Ta-Fu Wang, Chien-Lun Huang, Jia-Chi Wang, Liang-Yi Lin, and Pei-
775 Hsin Liang for assisting with the nucleus size quantification. We thank Drs. Darren
776 Williams, Brian Calvi, Guang-Chao Chen, Bloomington *Drosophila* Stock Center, Kyoto
777 Stock Center, Vienna *Drosophila* RNAi Center, and Fly Core Taiwan for generously
778 providing fly strains. We thank the Image Core of the Brain Research Center and the
779 Confocal Imaging Core at National Tsing Hua University for assistance with confocal
780 microscopy. We are grateful to Drs. Jui-Chou Hsu, Guang-Chao Chen, and Tim Tully for
781 their helpful comments and discussion regarding this work. This work was supported by
782 grants from the Ministry of Science and Technology of Taiwan (106-2811-B-007-008
783 and 109-2311-B-007-003), and the Higher Education Sprout Project, funded by the
784 Ministry of Science and Technology and the Ministry of Education of Taiwan.

785

786 **Author contributions**

787 Ya-Chu Chang and Tzu-Kang Sang conceived and designed the experiments. Ya-Chu
788 Chang, Yu-Xiang Peng, Chao-Jie Shih and Tzu-Kang Sang performed the experiments.
789 Ya-Chu Chang, Yu-Xiang Peng, Chao-Jie Shih, and Tzu-Kang Sang analyzed the data.
790 Ya-Chu Chang, Henry C Chang, and Tzu-Kang Sang wrote the paper.

791

792 **Competing interests**

793 The authors declare no competing interests.

794

795

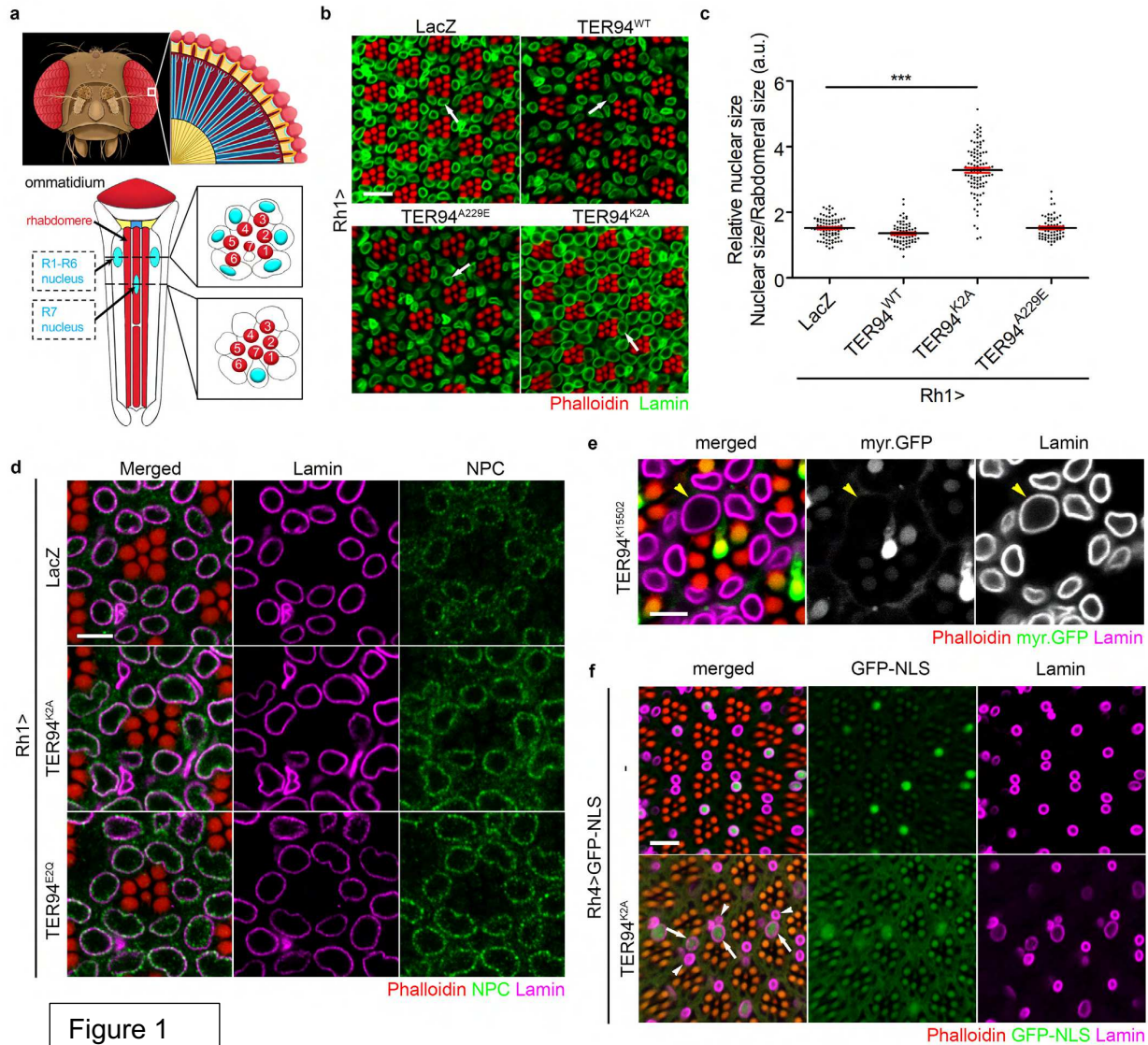


Figure 1

796

797 **Figure 1. Loss of TER94 function induces nuclear expansion.** **a** A cartoon depiction of
 798 *Drosophila* compound eye. The specialized photon-detecting rhabdomere and the proximal
 799 positions of R1-R7 nuclei are indicated. Two cross-section sketches indicated by dash lines
 800 show R1-R6 and R7 nuclei with the corresponding rhabdomeres. **b** Confocal images of 5-day-
 801 old adult retinas from flies expressing indicated transgenes under the control of *Rh1-GAL4*
 802 stained with phalloidin (red) and anti-Lamin (green) antibody to visualize the rhabdomeres and
 803 the nuclear envelope, respectively. The arrows indicate representative examples of nuclei in
 804 each genotype. **c** Quantification of the nuclear area of R1-R6 from flies of indicated genotypes.

805 67-96 nuclei from ≥ 4 independent eyes are measured in each group. Each dot represents an
806 independent R cell. Values shown represent mean (black line) \pm SE (red line). *** $p < 0.001$ as
807 compared to *Rh1>LacZ* (one-way ANOVA with Bonferroni's multiple comparison test). **d**
808 Confocal images of 5-day-old adult retinas expressing indicated transgenes under the control of
809 *Rh1-GAL4*. The retinas are stained with phalloidin (red), anti-Lamin (magenta), and anti-NPC
810 (green) antibodies. The anti-Lamin and anti-NPC signals are shown separately from the merged
811 images for comparison. **e** An adult eye bearing *TER94^{K15502}* clone is stained with phalloidin (red)
812 and anti-Lamin (magenta) antibody. The absence of myr.GFP marks somatic clone
813 homozygous for *TER94^{K15502}* as the arrowhead indicated. The myr.GFP and anti-Lamin are
814 shown separately from the merged image and converted to black and white for comparison. **f**
815 Confocal images of 5-day-old adult retinas expressing GFP-NLS (green) alone (-) or co-
816 expressing GFP-NLS and *TER94^{K2A}* under the control of *Rh4-GAL4* stained with phalloidin (red)
817 and anti-Lamin (magenta) antibody. *Rh4-GAL4* is active in a subset of R7 photoreceptors, which
818 are indicated by the presence of GFP-NLS. The GFP-NLS and anti-Lamin signals are shown
819 separately from the merged images for comparison. The arrows indicate the enlarged nuclei of
820 R7 with the expression of GFP-NLS and *TER94^{K2A}*, and the arrowheads indicate the normal
821 nuclei in R7 without transgenes expression. Scale bars: 10 μm (**b, f**), 5 μm (**d, e**).
822

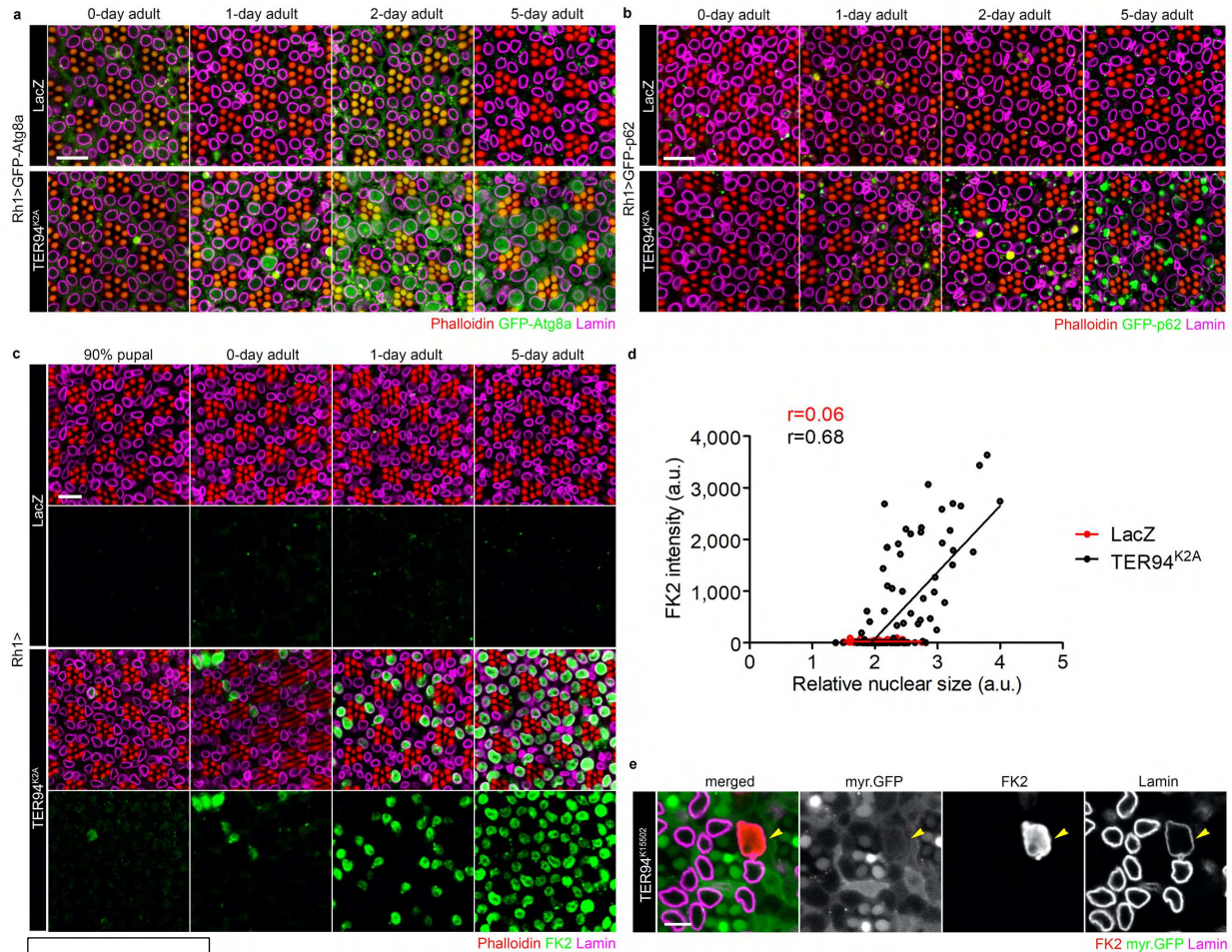


Figure 2

823
824

825 **Figure 2. Atg8, p62, and ubiquitinated nuclear proteins accumulate in cells lacking TER94**
826 **function. a, b** *Drosophila* retinas from freshly-eclosed (0-day) to 5-day-old adults co-expressing
827 GFP-Atg8a with LacZ (control) or TER94^{K2A} (a) or GFP-p62 with LacZ or TER94^{K2A} (b) under
828 the control of *Rh1-GAL4* are stained with phalloidin (red) and anti-Lamin (magenta) antibody. c
829 Time-course analysis of the change in nuclear size and the presence of ubiquitinated proteins
830 from late pupal to the 5-day-old adult stage. Pupal or adult eyes expressing LacZ or TER94^{K2A}
831 by *Rh1-GAL4* are stained with phalloidin (red), anti-Lamin (magenta), and anti-Ubiquitin
832 conjugates (FK2, green) antibodies. The signals of FK2 staining are separated from the merged
833 images for comparison. d Pearson's correlation analysis of nuclear size and FK2 intensity.
834 Images of 1-day-old adult retina, as shown in panel c, are analyzed. 88-125 nuclei from ≥ 4

835 independent eyes are measured, and the r values represent Pearson's correlation coefficient in
836 each group. **e** An adult eye bearing *TER94*^{K15502} clone is stained with anti-Lamin (magenta) and
837 anti-Ubiquitin conjugates (FK2, red) antibodies. The absence of myr.GFP marks somatic clone
838 homozygous for *TER94*^{K15502} as the arrowhead indicated. The myr.GFP, anti-Lamin, and FK2
839 signals are shown separately from the merged image and converted to black and white for
840 comparison. Scale bars: 10 μm (**a-c**), 5 μm (**e**).

841

842

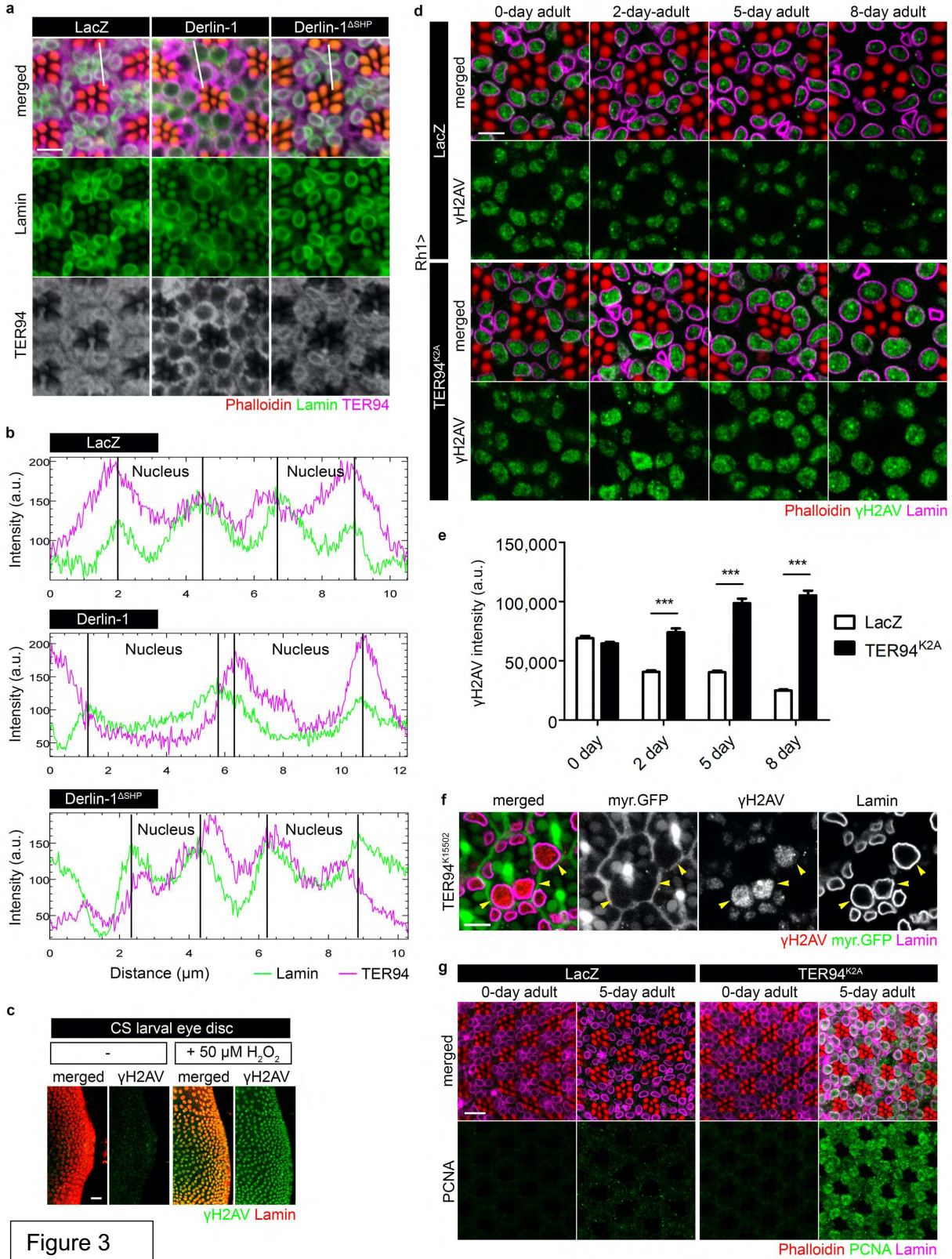
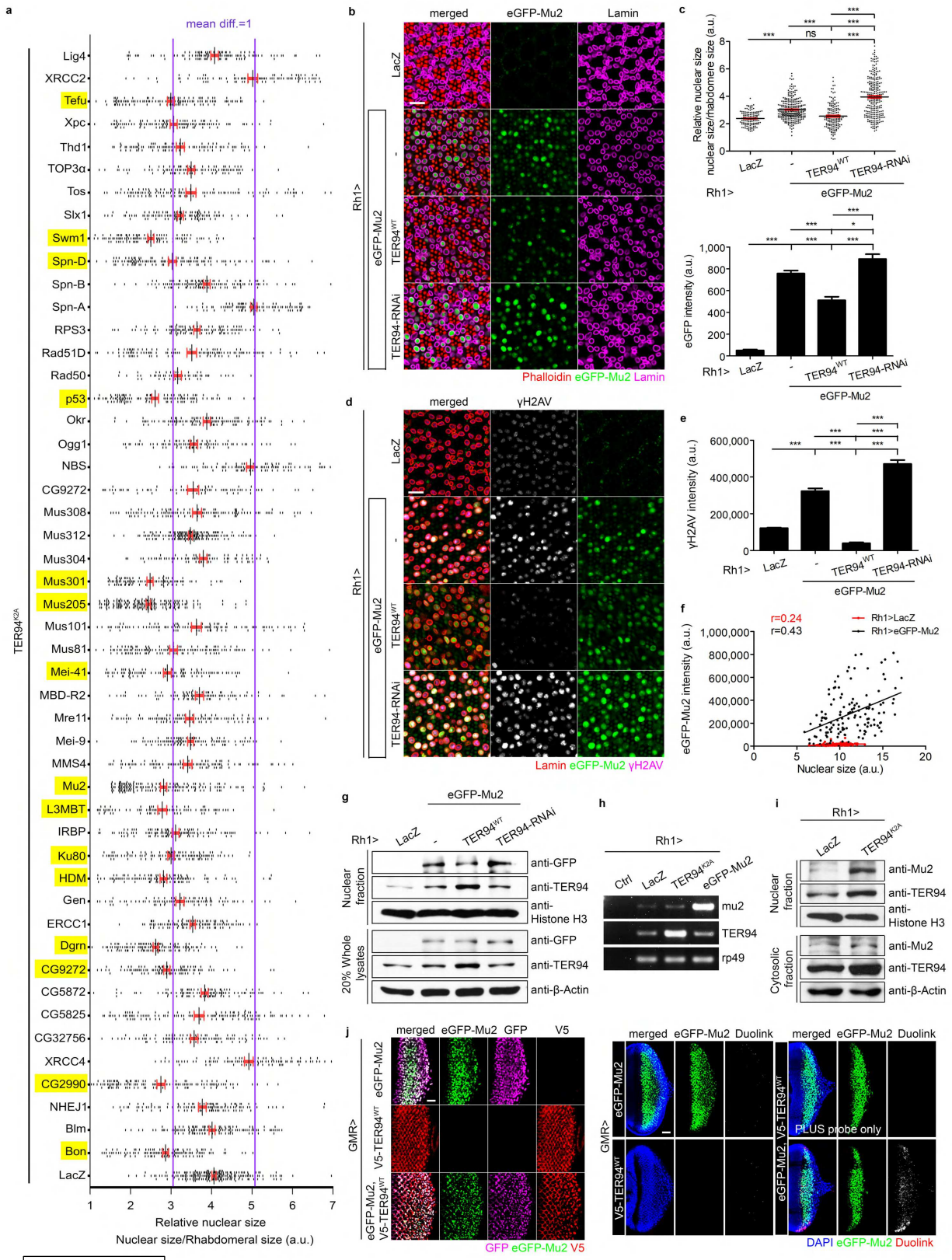


Figure 3

844 **Figure 3. Blocking TER94 function hampers DNA damage repair.** **a** Confocal images of 5-
845 day-old adult retinas expressing indicated transgenes by *Rh1-GAL4*. The retinas are stained
846 with phalloidin (red), anti-Lamin (green), and anti-TER94 (magenta) antibodies. The anti-Lamin
847 and anti-TER94 signals are shown separately from the merged images for comparison. The
848 anti-TER94 signals are converted to black and white for illustrating the subcellular distribution of
849 TER94. **b** Analysis of TER94 subcellular distribution. The analyzing range is randomly chosen
850 by drawing a line across two nuclei in each group as the white lines shown in panel (a). Image J
851 measures the intensities of anti-Lamin and anti-TER94 signals along the lines. The peaks of the
852 anti-Lamin signal define the borders of the nuclei. **c** Confocal images of normal larval eye discs
853 (Canton S; CS) with or without the treatment of DNA damaging agent, 50 μ M H₂O₂. Anti-Lamin
854 (red) and anti- γ H2AV (green) antibodies are used to mark the nuclear envelope and the DNA
855 damage sites. **d** Time-course analysis of the change in nuclear size and the level of γ H2AV
856 from freshly eclosed (0-day) to 8-day-old adult stage. Adult eyes expressing LacZ (control) or
857 TER94^{K2A} by *Rh1-GAL4* are stained with phalloidin (red), anti-Lamin (magenta), and anti- γ H2AV
858 antibodies (green). **e** Quantification of the anti- γ H2AV signal intensity from flies of indicated
859 genotypes. 56-126 nuclei from ≥ 2 independent eyes are measured in each group. Values
860 shown represent mean \pm SE. *** $p < 0.001$ as compared to *Rh1>LacZ* of corresponding age (two-
861 way ANOVA with Bonferroni post-test). **f** An adult eye bearing *TER94*^{K15502} clone is stained with
862 anti-Lamin (magenta) and anti- γ H2AV (red) antibodies. The absence of myr.GFP marks somatic
863 clone homozygous for *TER94*^{K15502} as the yellow arrowheads indicated. The myr.GFP, anti-
864 Lamin, and anti- γ H2AV signals are shown separately from the merged image and converted to
865 black and white for comparison. **g** Confocal images of adult retinas from flies of the indicated
866 ages expressing LacZ or TER94^{K2A} by *Rh1-GAL4* stained with phalloidin (red), anti-Lamin
867 (magenta), and anti-PCNA (green) antibodies. Scale bars: 5 μ m (a, d, f), 20 μ m (c), 10 μ m (g).
868



869

Figure 4

870

871 **Figure 4. TER94 influences Mu2 level in regulating nuclear size.** **a** Quantification of the R1-
872 R6 nuclear area from flies of indicated genotypes. 56-212 nuclei from ≥ 2 independent eyes are
873 measured in each group. The purple lines indicate the difference of the mean equals 1 (mean
874 diff. =1) as compared to the control (*Rh1>TER94^{K2A}, LacZ*). The DDR genes with mean diff. ≥ 1
875 are marked in yellow. **b** Confocal images of 7-day-old adult retinas from flies expressing
876 indicated transgenes under the control of *Rh1-GAL4* stained with phalloidin (red) and anti-Lamin
877 (magenta) antibody. **c** Quantification of the R1-R6 nuclear area (upper panel, 126-277 nuclei
878 from ≥ 4 independent eyes are measured in each group) or eGFP intensity (lower panel, 95-267
879 nuclei from ≥ 4 independent eyes are measured in each group). **d** Confocal images of 7-day-old
880 adult retinas from flies expressing indicated transgenes under the control of *Rh1-GAL4* stained
881 with anti-Lamin (red) and anti- γ H2AV (magenta) antibodies. **e** Quantification of the anti- γ H2AV
882 intensity. 114-268 nuclei from ≥ 3 independent eyes are measured in each group. **f** Pearson's
883 correlation analysis of nuclear size and eGFP-Mu2 intensity. 134-150 nuclei from ≥ 3
884 independent eyes are measured, and the r values represent Pearson's correlation coefficient in
885 each group. **g** Western analysis of eGFP-Mu2 level (detected by anti-GFP antibody) in TER94
886 overexpression (TER94^{WT}) or knockdown (TER94-RNAi) backgrounds. The anti-Histone H3 and
887 the anti- β -Actin serve as loading controls for the nuclear and the whole protein lysates. **h** RT-
888 PCR measurement of the transcriptional level of *mu2* and *TER94* from flies expressing indicated
889 genotypes. The control (Ctrl) groups contain all the PCR reaction reagents except the cDNA
890 templates. The level of rp49 serves as an internal control. **i** Western analysis of endogenous
891 Mu2 level in tissues expressing LacZ (control) or TER94^{K2A}. The detection of anti-Histone H3
892 and anti- β -Actin serve as loading controls for the nuclear and the cytosolic protein lysates. **j**
893 Larval eye discs from flies expressing indicated transgenes under the control of *GMR-GAL4* are
894 stained with anti-GFP (magenta) and anti-V5 (red) antibodies (left panel). Larvae bearing the
895 same genotypes are subjected to *in situ* PLA using anti-GFP and anti-V5 antibodies (right
896 panel). The duolink signal reveals proteins in the same complex. The lines in dot plots from **a**, **c**

897 represent mean (black) \pm SE (red). The bar charts from **c**, **e** represent mean \pm SE. ns, not
898 significant, * $p < 0.05$, *** $p < 0.001$ as compared with indicated genotypes (one-way ANOVA with
899 Bonferroni's multiple comparison test). Scale bars: 10 μm (**b**, **d**), 20 μm (**j**).

900

901

902

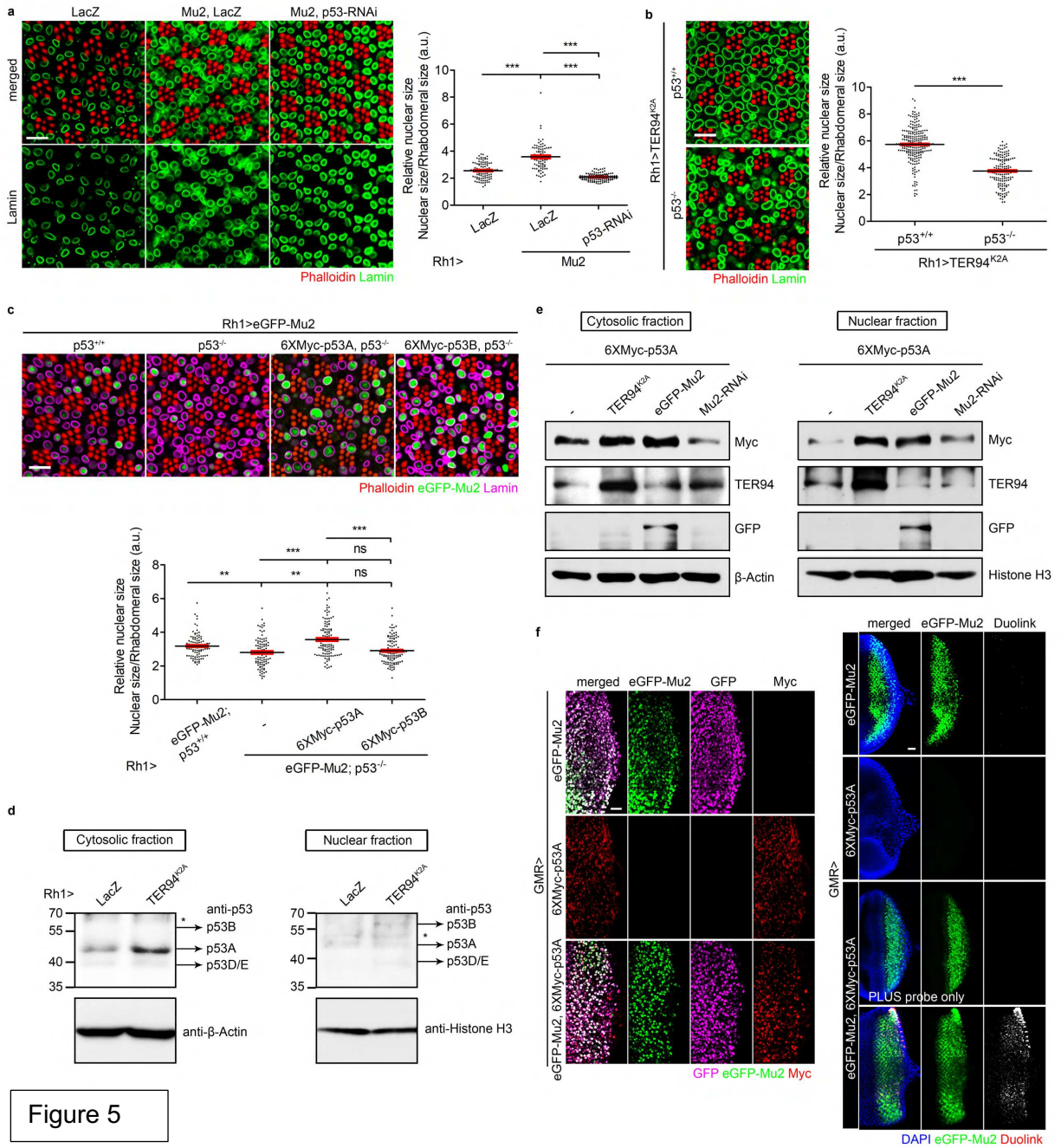


Figure 5

903

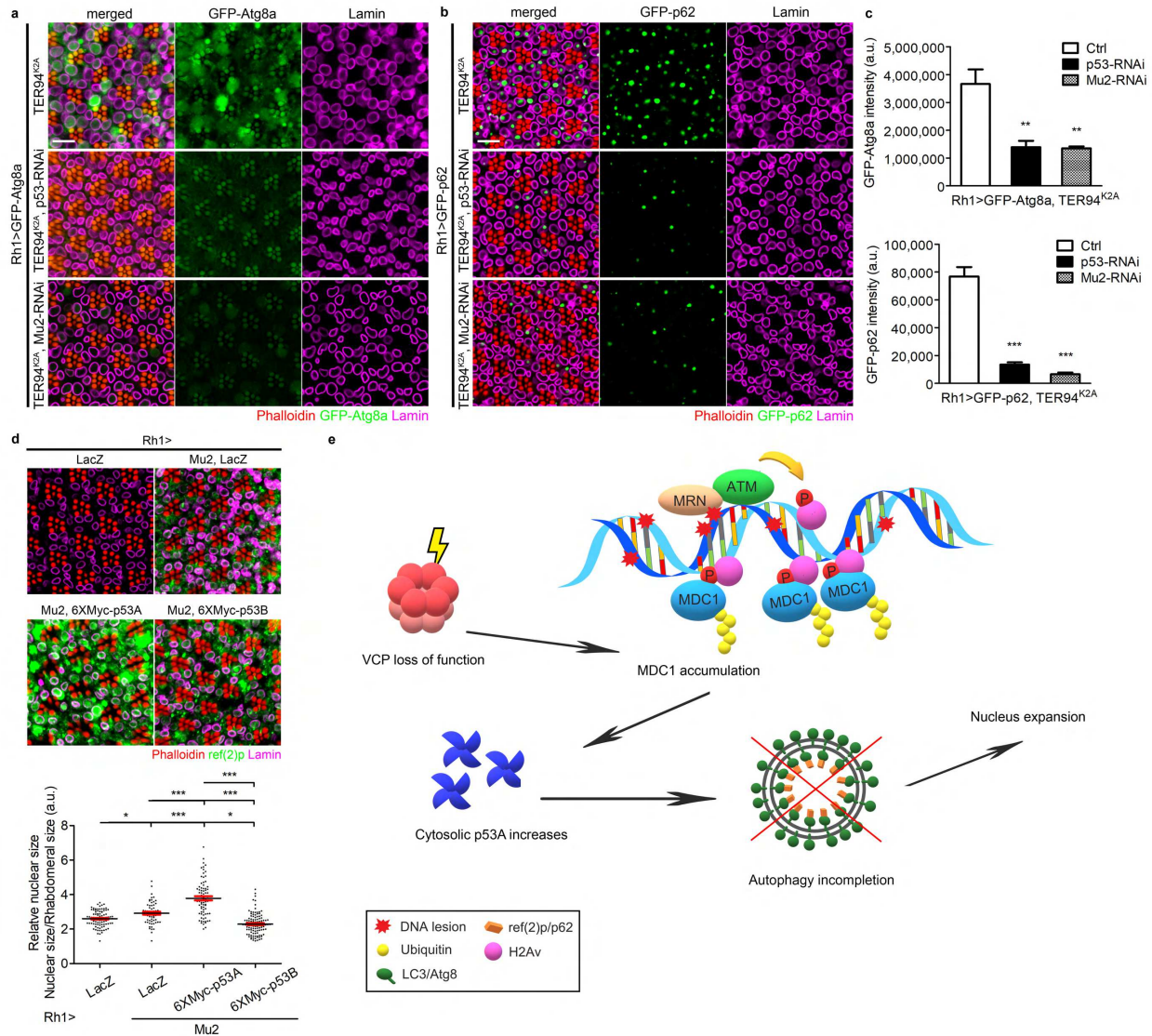
904 **Figure 5. p53 acts downstream of Mu2 in TER94 dysfunction-induced nuclear expansion.**

905 **a** Confocal micrographs of 5-day-old control (*Rh1>LacZ*) or *Rh1>Mu2* adult retina co-expressing
 906 LacZ or p53-RNAi stained with phalloidin (red) and anti-Lamin (magenta) antibody (left panel).

907 Quantification of R1-R6 nuclear area from 80-110 nuclei (≥ 3 independent eyes) are measured

908 in each group (right panel). **b** Confocal images of 6-day-old *Rh1>TER94^{K2A}* adult retina in wild

909 type (+/+) or *p53* null (-/-) background stained with phalloidin (red) and anti-Lamin (green)
910 antibody (left panel). Quantification of R1-R6 nuclear area from 149-219 nuclei (≥ 5 independent
911 eyes) are measured in each group (right panel). **c** Confocal micrographs of 5-day-old *Rh1>Mu2*
912 adult retina in wild type (+/+), *p53* null (-/-), 6XMyC-p53A overexpression in *p53* null (-/-), and
913 6XMyC-p53B overexpression in *p53* null (-/-) backgrounds stained with phalloidin (red) and anti-
914 Lamin (magenta) antibody (upper panel). Quantification of R1-R6 nuclear area from 80-116
915 nuclei (≥ 3 independent eyes) are measured in each group (lower panel). The lines in dot plots
916 from **a-c** represent mean (black) \pm SE (red). ns, not significant, ** $p < 0.01$, *** $p < 0.001$ student's t-
917 test, two-tailed (**b**), one-way ANOVA with Bonferroni's multiple comparison test (**a**, **c**). **d**
918 Western analysis of the cytosolic and the nuclear *p53* level in tissues expressing LacZ (control)
919 or TER94^{K2A} under the control of *Rh1-GAL4*. The arrows indicate distinct *p53* isoforms
920 according to their molecular weights and the asterisks mark nonspecific bands. **e** Larval eye
921 discs expressing indicated genes are stained with anti-GFP (magenta) and anti-Myc (red)
922 antibodies (left panel). Larvae bearing the same genotypes are subjected to *in situ* PLA using
923 anti-GFP and anti-Myc antibodies (right panel). The duolink signal reveals proteins in the same
924 complex. **f** Western analysis of the Myc-p53A level in tissues expressing indicated genes. Scale
925 bars: 10 μm (**a-c**), 20 μm (**e**).
926



927

928

929 **Figure 6. TER94 dysfunction triggers nuclear expansion through p53A-mediated**

930 **autophagy blockage. a, b** Confocal micrographs of 7-day-old *Rh1>TER94^{K2A}>GFP-Atg8a* (a)

931 or *Rh1>TER94^{K2A}>GFP-p62* (b) adult retinas co-expressing p53-RNAi or Mu2-RNAi stained

932 with phalloidin (red) and anti-Lamin (magenta) antibody. c Quantification of the GFP-Atg8a

933 (upper panel) or the GFP-p62 (lower panel) intensity; at least 4 independent eyes are measured

934 in each group. d Confocal micrographs of 5-day-old adult retina expressing LacZ alone

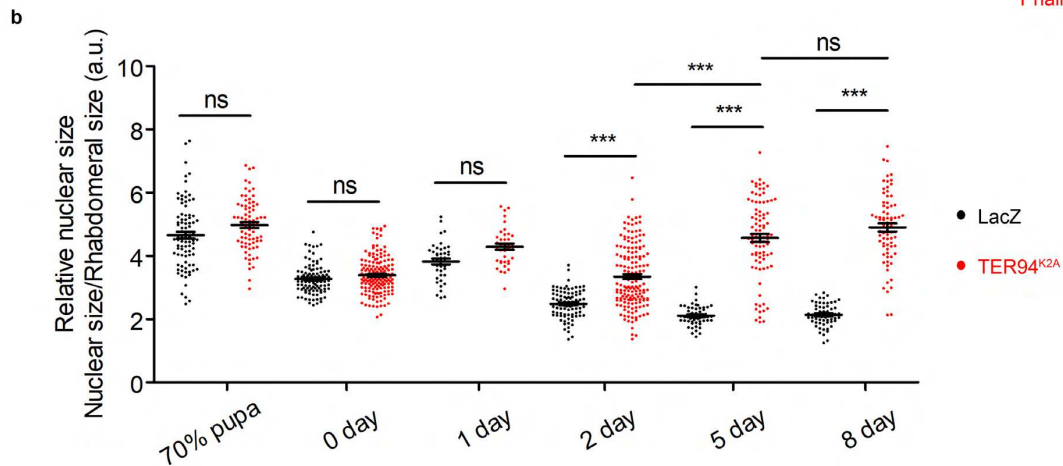
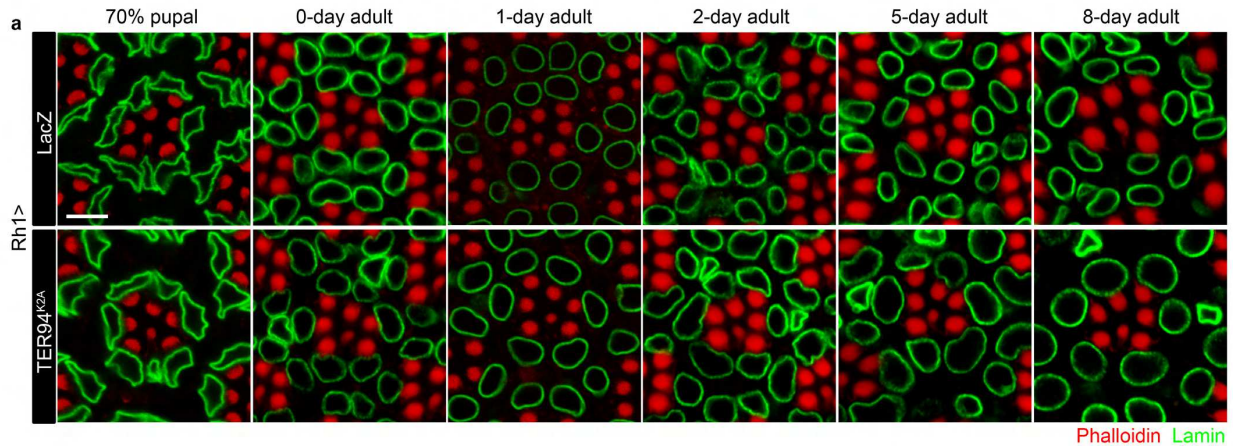
935 (control), co-expressing Mu2 with LacZ or 6XMyc tagged p53 isoforms by *Rh1-GAL4* stained

936 with phalloidin (red), anti-Lamin (magenta), and anti-ref(2)p antibodies (upper panel).
937 Quantification of R1-R6 nuclear area from 58-96 nuclei (from ≥ 2 independent eyes) are
938 measured in each group (lower panel). Scale bars: 10 μm (**a**, **b**, **d**). Values represent mean \pm
939 SE. * $p < 0.05$, ** $p < 0.01$, *** $p < 0.001$ (one-way ANOVA with Bonferroni's multiple comparison test)
940 (**c**, **d**). **e** A model for how loss of VCP function triggers MDC1-p53-mediated autophagy
941 blockage and nuclear expansion. Initially, the MRN complexes recognize DNA lesions and
942 recruit ATM to the damaged sites. The histone variant H2AV near the damaged sites are
943 phosphorylated by ATM, resulting in γH2AV , which recruits MDC1. Serving as a signaling
944 platform, MDC1 interacts with numerous DNA damage signaling or repairing proteins, including
945 p53. VCP should tightly control the level and the retention period of MDC1 on the injured DNA
946 normally. However, loss of TER94's activity leads to an accumulation of MDC1 and prolongs the
947 interaction between MDC1 and p53, which stabilizes p53, especially p53A. The increased p53A
948 in the cytosol prohibits autophagy flux, which ultimately causes nuclear expansion.
949

950 **Table 1. Primer sets used in RT-PCR.**

Targeting cDNA	Sequences of primers
rp49	F: 5'-CCAGTCGGATCGATATGCTAA-3'
	R: 5'-ACGTTGTGCACCAGGAACTT-3'
TER94	F: 5'-GTGTTTCATCATCGGAGCCAC-3'
	R: 5'-GGATCGTCCTCGTCCATGTC-3'
Mu2	F: 5'-GCACGTGGTGGAGATCAC-3'
	R: 5'-CGTACAGATCCACGCTGATG-3'

951



952

953

Supplementary Figure 1

954

Supplementary Figure 1. Developmental changes in the morphology and size of outer

955

photoreceptor cell nuclei. a Time-course analysis of the change in nuclear morphology and

956

size from 70% pupal to the 8-day-old adult stage. Pupal or adult eyes expressing LacZ (control)

957

or TER94^{K2A} by *Rh1-GAL4* are stained with phalloidin (red) and anti-Lamin (green) antibody. **b**

958

Quantification of the nuclear area of R1-R6 from flies of indicated genotypes. 39-162 nuclei from

959

≥ 2 independent eyes are measured in each group. The horizontal lines shown in **b** represent

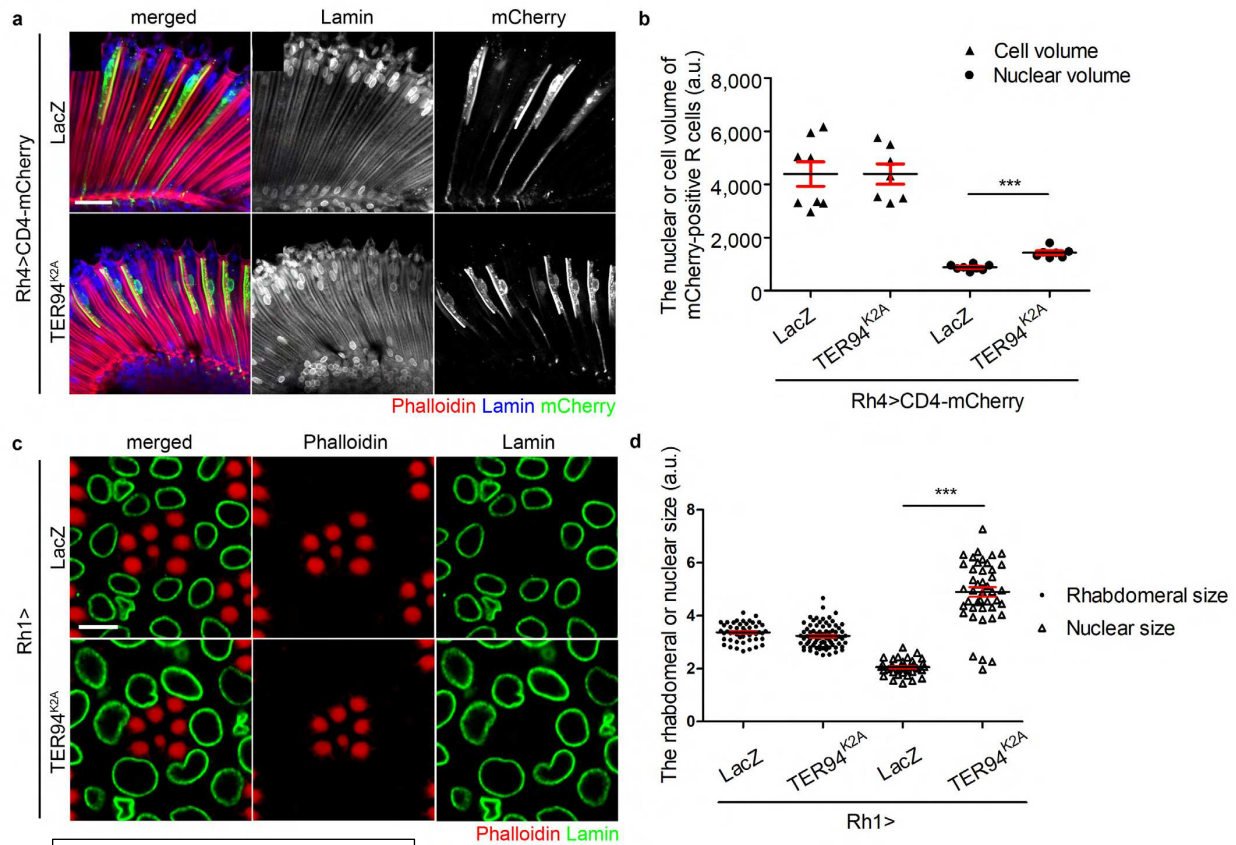
960

mean ± SE. ns, not significant, ***p<0.001 (one-way ANOVA with Bonferroni's multiple

961

comparison test). Scale bar: 5 μm (**a**).

962



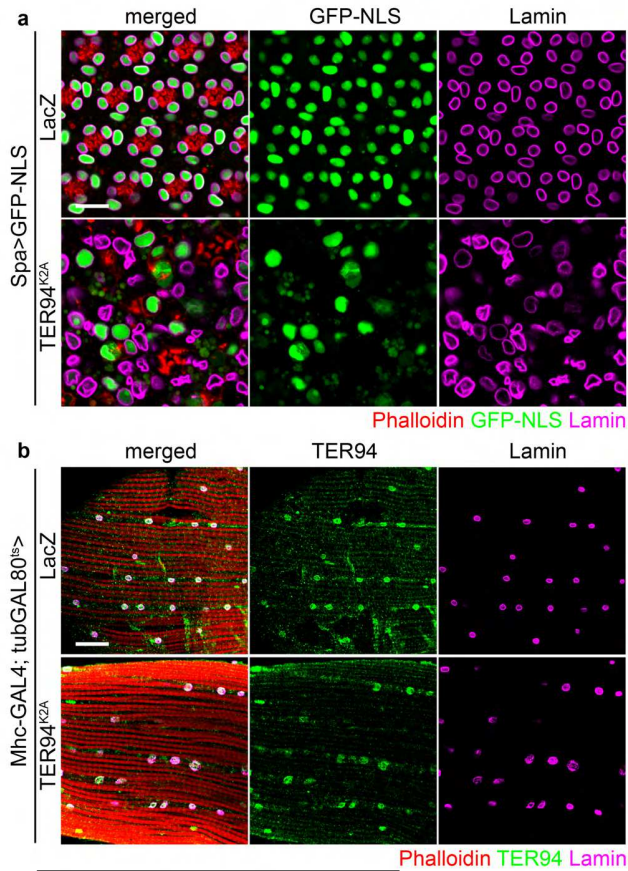
Supplementary Figure 2

963

964

965 **Supplementary Figure 2. Loss of TER94 function increases the nuclear size without**
 966 **altering the overall cell volume.** **a** Confocal images of 3-day-old adult retinas co-expressing
 967 CD4-mCherry with LacZ (control) or TER94^{K2A} under the control of *Rh4-GAL4* stained with
 968 phalloidin (red), anti-mCherry (green), and anti-Lamin (blue) antibodies to visualize the
 969 rhabdomeres, the cytoplasmic membrane, and the nuclear envelope, respectively. The anti-
 970 Lamin and anti-mCherry signals are shown separately from the merged images and converted
 971 to black and white for comparison. **b** Quantification of the cellular or nuclear volume of R7 cells
 972 labeled by mCherry from flies co-expressing LacZ or TER94^{K2A}. The cellular or nuclear volume
 973 are manually outlined according to the mCherry or anti-Lamin signals respectively as shown in
 974 **(a)** and measured by Image J. 7-8 R7 cells from ≥ 4 eyes are measured in each group. **c**
 975 Confocal images of 5-day-old adult retinas expressing LacZ or TER94^{K2A} under the control of

976 *Rh1-GAL4* stained with phalloidin (red) and anti-Lamin (green) antibody. **d** Quantification of the
977 rhabdomeral or nuclear area of R1-R6 nuclei from flies expressing LacZ or TER94^{K2A}. 37-80
978 nuclei (≥ 2 independent eyes) are measured in each group. The lines represent mean (black) \pm
979 SE (red). *** $p < 0.001$ (student's t test, two-tailed). Scale bars: 20 μm (**a**), 5 μm (**d**).
980



Supplementary Figure 3

981

982

983 **Supplementary Figure 3. TER94 dysfunction induces nuclear size increase in cone cells**

984 **and indirect flight muscle cells. a** Confocal images of late pupal retinas co-expressing GFP-

985 NLS with LacZ (control) or TER94^{K2A} in cone cells under the control of *Spa-GAL4* stained with

986 phalloidin (red) and anti-Lamin (magenta) antibody to visualize the rhabdomeres and the

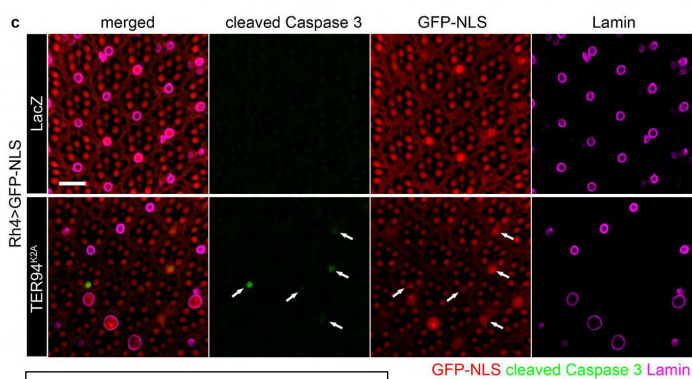
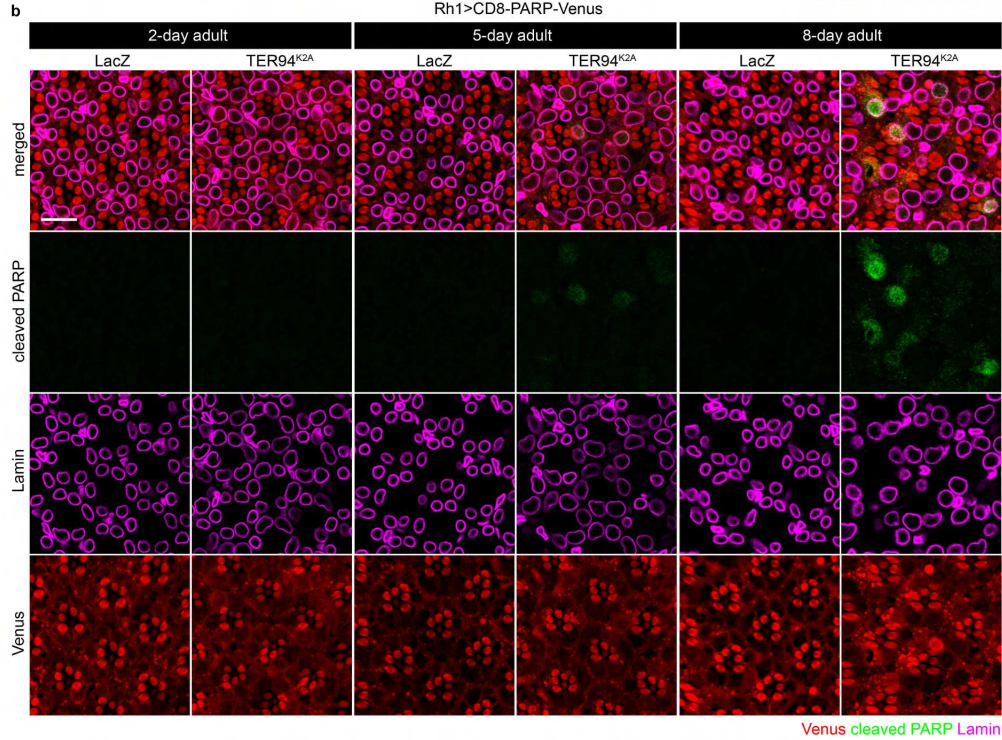
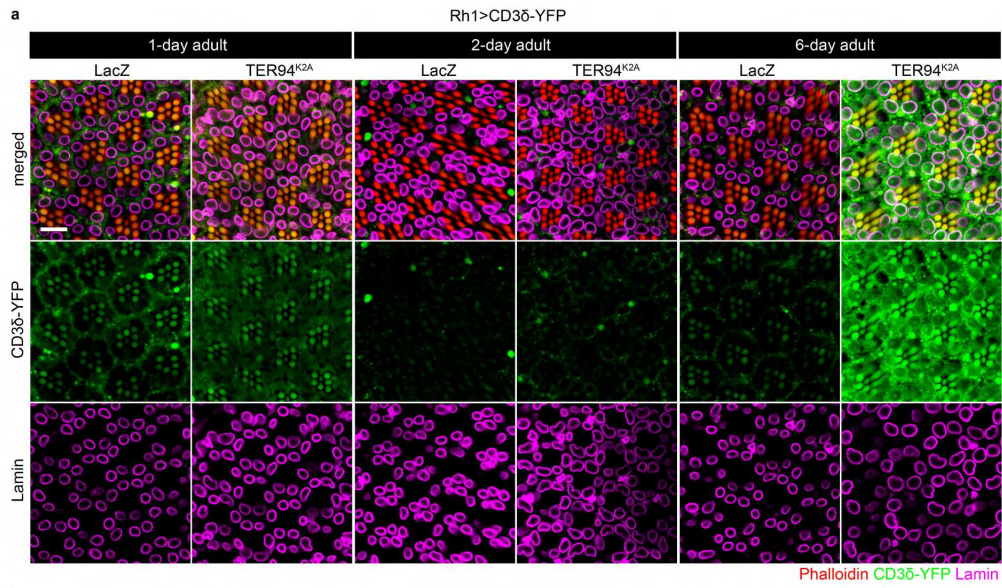
987 nuclear envelope, respectively. GFP-NLS indicates the cone cell nuclei in the retina. **B** Adult

988 indirect flight muscles expressing LacZ or TER94^{K2A} by *Mhc-GAL4; tub-GAL80^{ts}* are stained with

989 phalloidin (red), anti-Lamin (magenta), and anti-TER94 (green) antibodies. Flies raised at 18°C

990 are transferred to 30°C after eclosion for 3 weeks to induce transgenes expression. Scale bar:

991 10 μm (a), 20 μm (b).

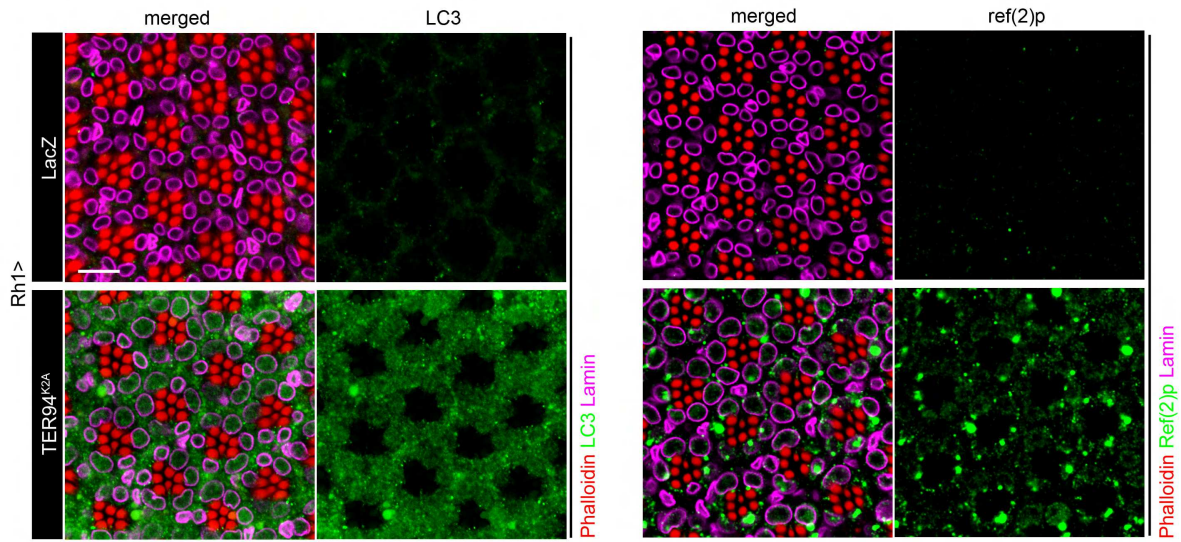


992

Supplementary Figure 4

993 **Supplementary Figure 4. TER94 dysfunction-caused nuclear expansion is not linked to a**
994 **failure in ERAD or apoptosis activation. a** Time-course analysis of the change in the nuclear
995 size and the signal of ERAD reporter, CD3 δ -YFP, from 1-day-old to 6-day-old adult stage. Adult
996 eyes co-expressing CD3 δ -YFP with LacZ (control) or TER94^{K2A} by *Rh1-GAL4* are stained with
997 phalloidin (red) and anti-Lamin (magenta) antibody. **b** Time-course analysis of the change in the
998 nuclear size and the signal of apoptotic reporter, cleaved PARP, from 2-day-old to 8-day-old
999 adult stage. Adult eyes co-expressing CD8-PARP-Venus with LacZ or TER94^{K2A} by *Rh1-GAL4*
1000 are stained with anti-cleaved PARP (green) and anti-Lamin (magenta) antibodies. The signals of
1001 Venus and anti-cleaved PARP are used to visualize the expression of the probe and caspase
1002 activation, respectively. **c** 5-day-old adult eyes co-expressing GFP-NLS with LacZ or TER94^{K2A}
1003 by *Rh4-GAL4* are stained with anti-cleaved caspase 3 (green) and anti-Lamin (magenta)
1004 antibodies. GFP-NLS marks the R7 cells with transgenes expression. The white arrows point
1005 out the cleaved caspase 3 staining in a small population of GFP-NLS-positive R7 cells. Scale
1006 bar: 10 μ m (**a-c**).
1007

1008



1009

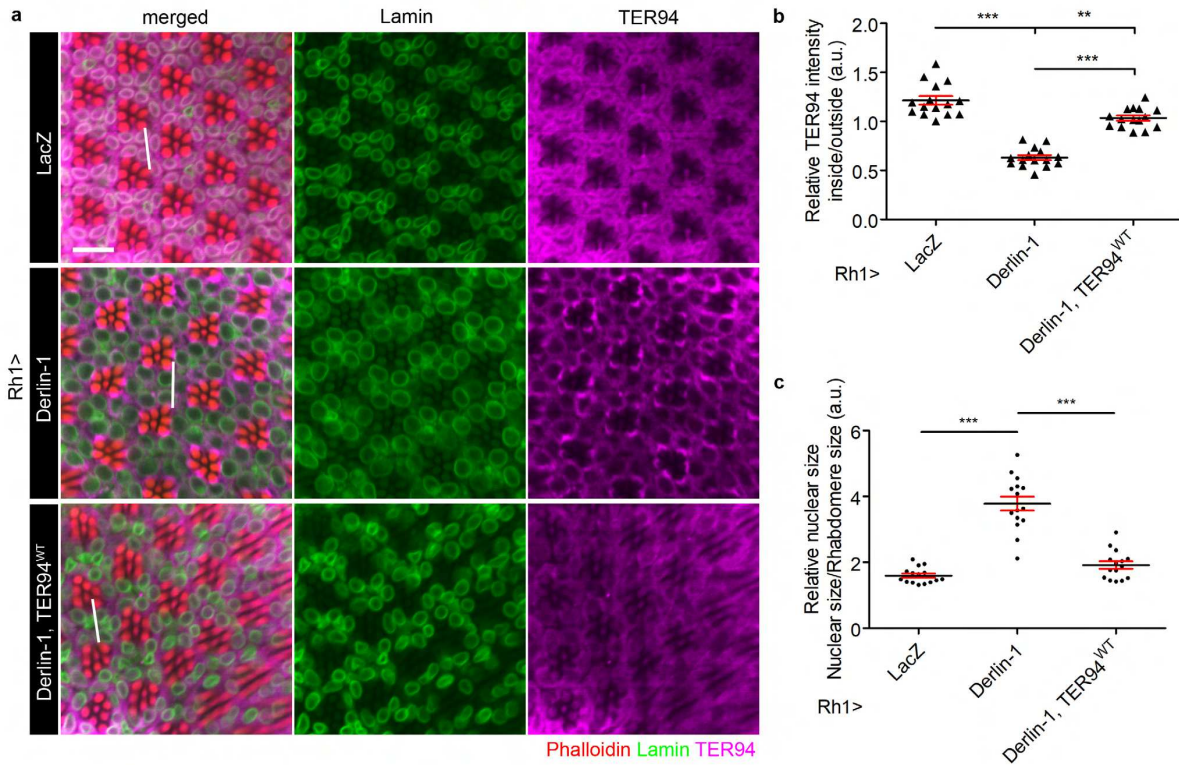
Supplementary Figure 5

1010

1011 **Supplementary Figure 5. LC3 and ref(2)p accumulate in TER94 dysfunction cells.** 5-day-
1012 old adult retinas expressing LacZ (control) or *TER94*^{K2A} by *Rh1-GAL4* are stained with phalloidin
1013 (red), anti-Lamin (magenta), and anti-LC3 (left, green) or anti-ref(2)p (right, green) antibodies.

1014 Scale bar: 10 μ m.

1015

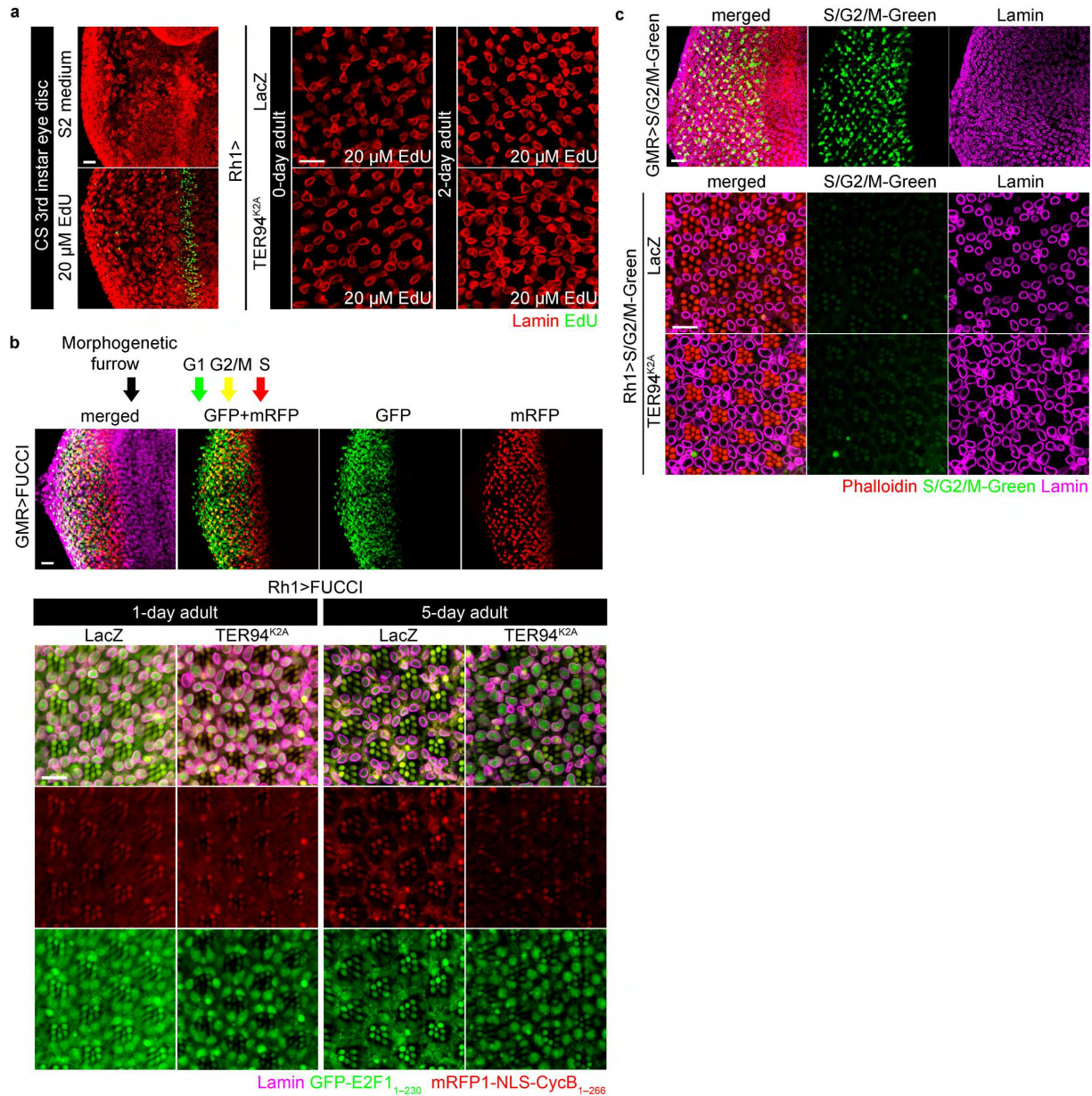


Supplementary Figure 6

1016
1017
1018
1019
1020
1021
1022
1023
1024
1025
1026
1027
1028
1029
1030

Supplementary Figure 6. Overexpressing TER94^{WT} suppresses Derlin-1-induced nuclear

expansion phenotype. **a** Adult eyes expressing LacZ (control), Derlin-1, or co-expressing Derlin-1 with TER94^{WT} by *Rh1-GAL4* are stained with phalloidin (red), anti-Lamin (green) and anti-TER94 (magenta) antibodies. The anti-Lamin and anti-TER94 signals are shown separately from the merged images for comparison. **b** Quantification of the relative anti-TER94 intensity inside versus outside the nucleus in tissues of indicated genotypes. The analyzing range is randomly chosen by drawing a line across two nuclei in each group as the white lines shown in **(a)**. The intensity of anti-Lamin and anti-TER94 signals along the lines is measured by Image J and the peaks of anti-Lamin signals are used to define the borders of the nuclei. 15 random analyzing regions from 3 independent eyes are measured in each group. **c** Quantification of the nuclear area of R1-R6 from flies of indicated genotypes. 15 nuclei from 3 independent eyes are measured in each group. The lines shown in **(b, c)** represent mean (black) \pm SE (red). ** $p < 0.01$, *** $p < 0.001$ (one-way ANOVA with Bonferroni's multiple comparison test). Scale bar: 10 μ m **(a)**.



1031

Supplementary Figure 7

1032

1033

Supplementary Figure 7. The nuclear expansion induced by TER94 dysfunction is not

1034

coupled to cell-cycle re-entry. a EdU cell proliferation assay. Images of 3rd instar Canton S

1035

(CS) larval eye discs (left panel) containing proliferating cells incubated with S2 medium

1036

(negative control) or 20 μ M EdU (positive control) for 1.5 hrs prior to fixation. The right panel

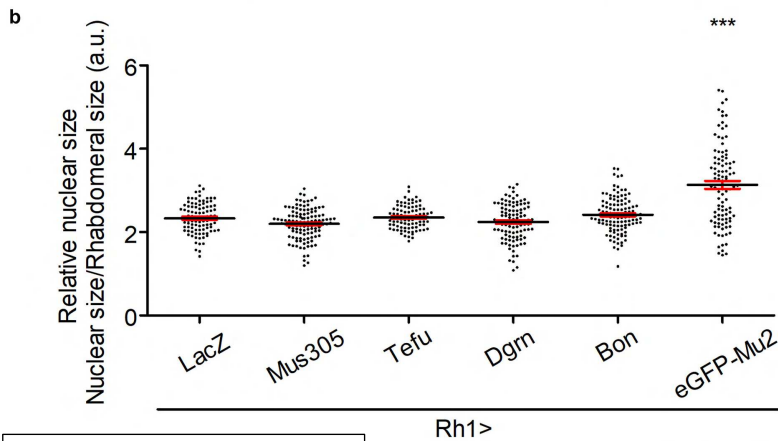
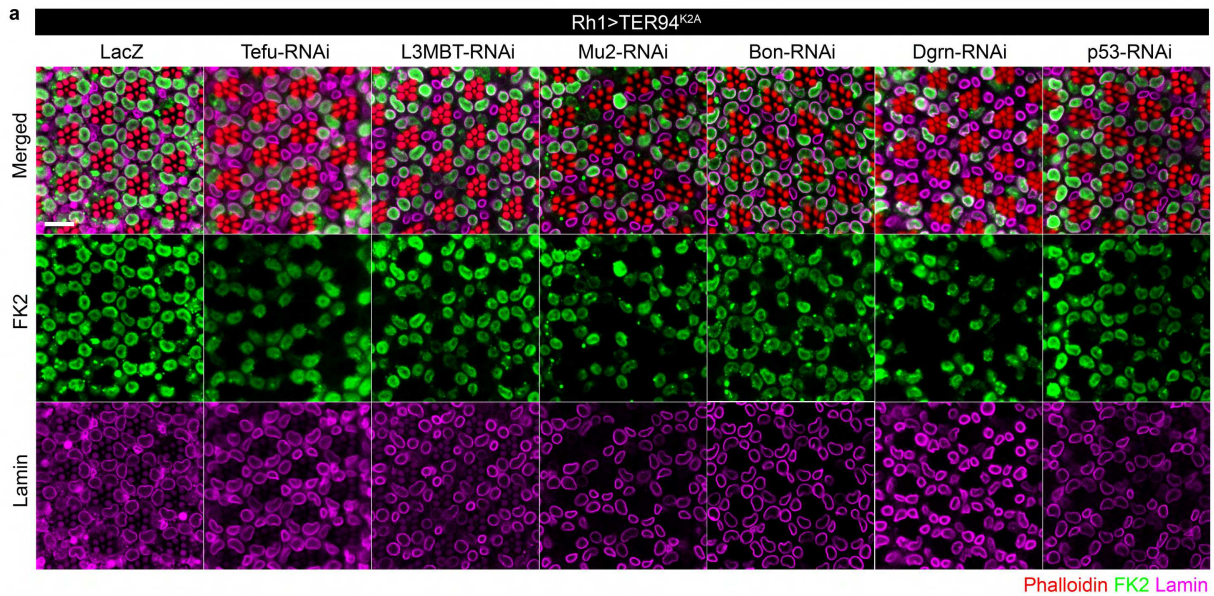
1037

shows adult retinas expressing LacZ or TER94^{K2A} by *Rh1*-GAL4 subjected to the EdU

1038

incorporation assay before (0-day, freshly-eclosed) and after (2-day) the nuclear expansion

1039 occurs. The anti-Lamin (red) antibody is used to mark the nuclear envelope and the Alexa
1040 Fluor[®] 488 azide (green) is used to detect the incorporated EdU. **b** Examination of the cell-cycle
1041 status with Fly-FUCCI, a fluorescent cell-cycle indicator composed of GFP-E2F1₁₋₂₃₀ and
1042 mRFP1-NLS-CycB₁₋₂₆₆. This technique differentially labels cells in the G1 (green; degradation of
1043 mRFP-tagged CycB), S (red; degradation of GFP-tagged E2F), and G2/M (yellow) phases.
1044 *GMR>Fly-FUCCI* larval eye discs (upper panel) show the cells behind the morphogenetic furrow
1045 in the S, G2/M, and G1 phases are labeled by green, yellow, and red fluorescence, respectively,
1046 as the corresponding arrows indicated. *Rh1>LacZ* or *Rh1>TER94^{K2A}* adult retinas (lower panel)
1047 co-expressing Fly-FUCCI before (1-day) and after (5-day) the nuclear expansion are stained
1048 with anti-Lamin (magenta) antibody to visualize the nuclear envelope. **c** Confocal micrographs
1049 of larval and adult eyes expressing S/G2/M-Green, a cell-cycle indicator labeling cells in the S,
1050 G2, or M phases of cell cycle with green fluorescence. Larval eye discs (upper panel)
1051 expressing S/G2/M-Green by *GMR-GAL4* are included as a positive control. Adult retinas (lower
1052 panel) co-expressing S/G2/M-Green with LacZ or TER94^{K2A} under the control of *Rh1-GAL4* are
1053 stained with phalloidin (red) and anti-Lamin antibody (magenta). Scale bar: 20 μm (**a-c** eye
1054 discs), 10 μm (**a-c** adult retinas).
1055



Supplementary Figure 8

1056

1057

Supplementary Figure 8. A genetic screen targeting DDR genes for ability to modify

1058

TER94 dysfunction-induced nuclear expansion. a Confocal images of 5-day-old adult retinas

1059

co-expressing TER94^{K2A} with LacZ (control) or the indicated RNAi constructs by *Rh1-GAL4*

1060

stained with phalloidin (red), anti-Lamin (magenta), and anti-ubiquitin-conjugates (FK2, green)

1061

antibodies. **b** Quantification of the nuclear area of R1-R6 from flies expressing the indicated

1062

genes by *Rh1-GAL4*. 90-117 nuclei (from ≥ 2 independent eyes) are measured in each group.

1063

The lines represent mean (black) \pm SE (red). *** $p < 0.001$ as compared to the control (*Rh1>LacZ*)

1064

(one-way ANOVA with Bonferroni's multiple comparison test). Scale bar: 10 μ m (**a**).

1065

Figures

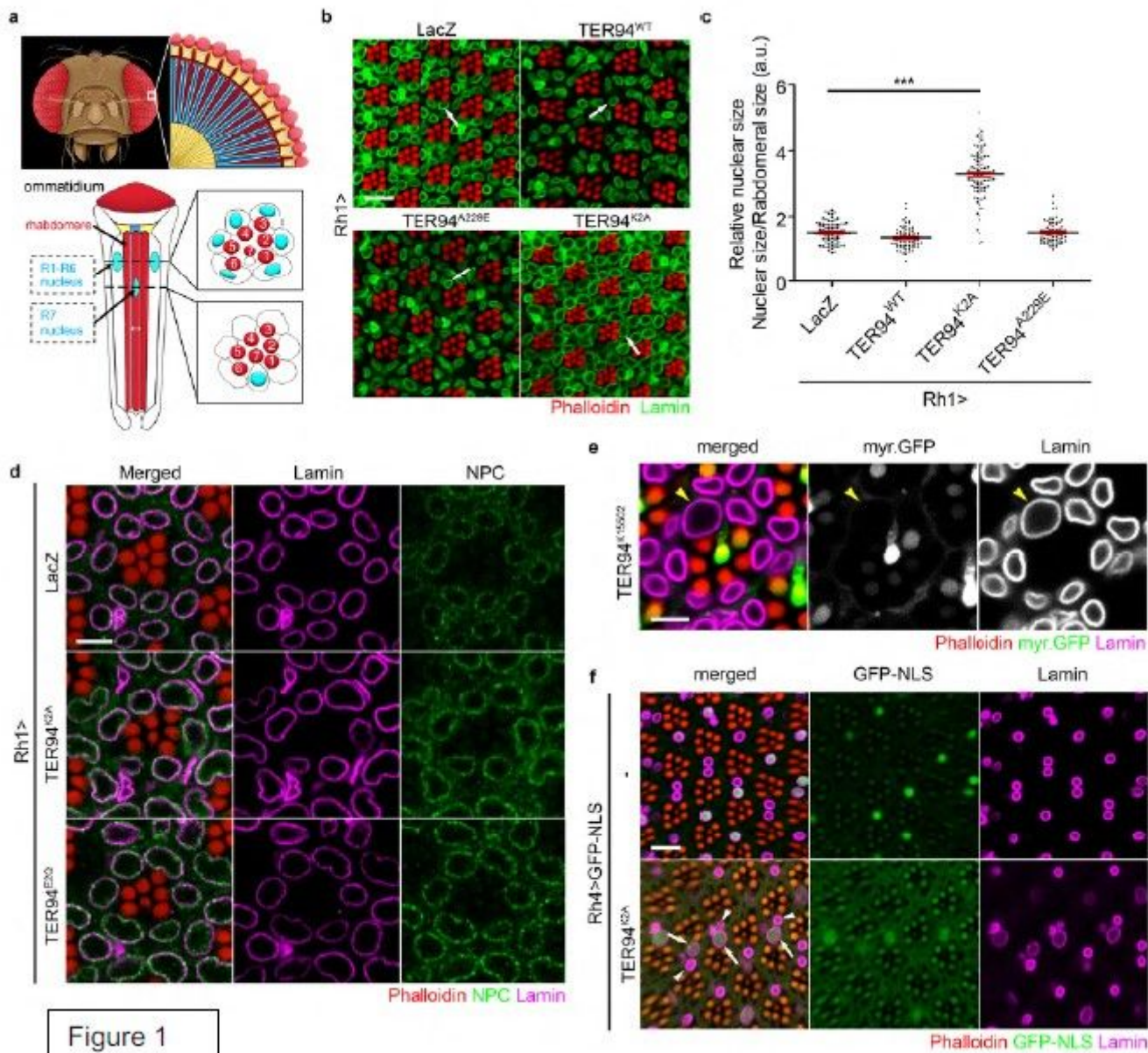


Figure 1

Figure 1

Loss of TER94 function induces nuclear expansion. **a** A cartoon depiction of *Drosophila* compound eye. The specialized photon-detecting rhabdomere and the proximal positions of R1-R7 nuclei are indicated. Two cross-section sketches indicated by dash lines show R1-R6 and R7 nuclei with the corresponding rhabdomeres. **b** Confocal images of 5-day old adult retinas from flies expressing indicated transgenes under the control of Rh1-GAL4 stained with phalloidin (red) and anti-Lamin (green) antibody to visualize the rhabdomeres and the nuclear envelope, respectively. The arrows indicate representative examples of nuclei in each genotype. **c** Quantification of the nuclear area of R1-R6 from flies of indicated genotypes. 67-96 nuclei from ≥ 4 independent eyes are measured in each group. Each dot represents an independent R cell. Values shown represent mean (black line) \pm SE (red line). *** $p < 0.001$ as compared to Rh1>LacZ

(one-way ANOVA with Bonferroni's multiple comparison test). d Confocal images of 5-day-old adult retinas expressing indicated transgenes under the control of Rh1-GAL4. The retinas are stained with phalloidin (red), anti-Lamin (magenta), and anti-NPC (green) antibodies. The anti-Lamin and anti-NPC signals are shown separately from the merged images for comparison. e An adult eye bearing TER94K15502 clone is stained with phalloidin (red) and anti-Lamin (magenta) antibody. The absence of myr.GFP marks somatic clone homozygous for TER94K15502 as the arrowhead indicated. The myr.GFP and anti-Lamin are shown separately from the merged image and converted to black and white for comparison. f Confocal images of 5-day-old adult retinas expressing GFP-NLS (green) alone (-) or co expressing GFP-NLS and TER94K2A under the control of Rh4-GAL4 stained with phalloidin (red) and anti-Lamin (magenta) antibody. Rh4-GAL4 is active in a subset of R7 photoreceptors, which are indicated by the presence of GFP-NLS. The GFP-NLS and anti-Lamin signals are shown separately from the merged images for comparison. The arrows indicate the enlarged nuclei of R7 with the expression of GFP-NLS and TER94K2A, and the arrowheads indicate the normal nuclei in R7 without transgenes expression. Scale bars: 10 μm (b, f), 5 μm (d, e).

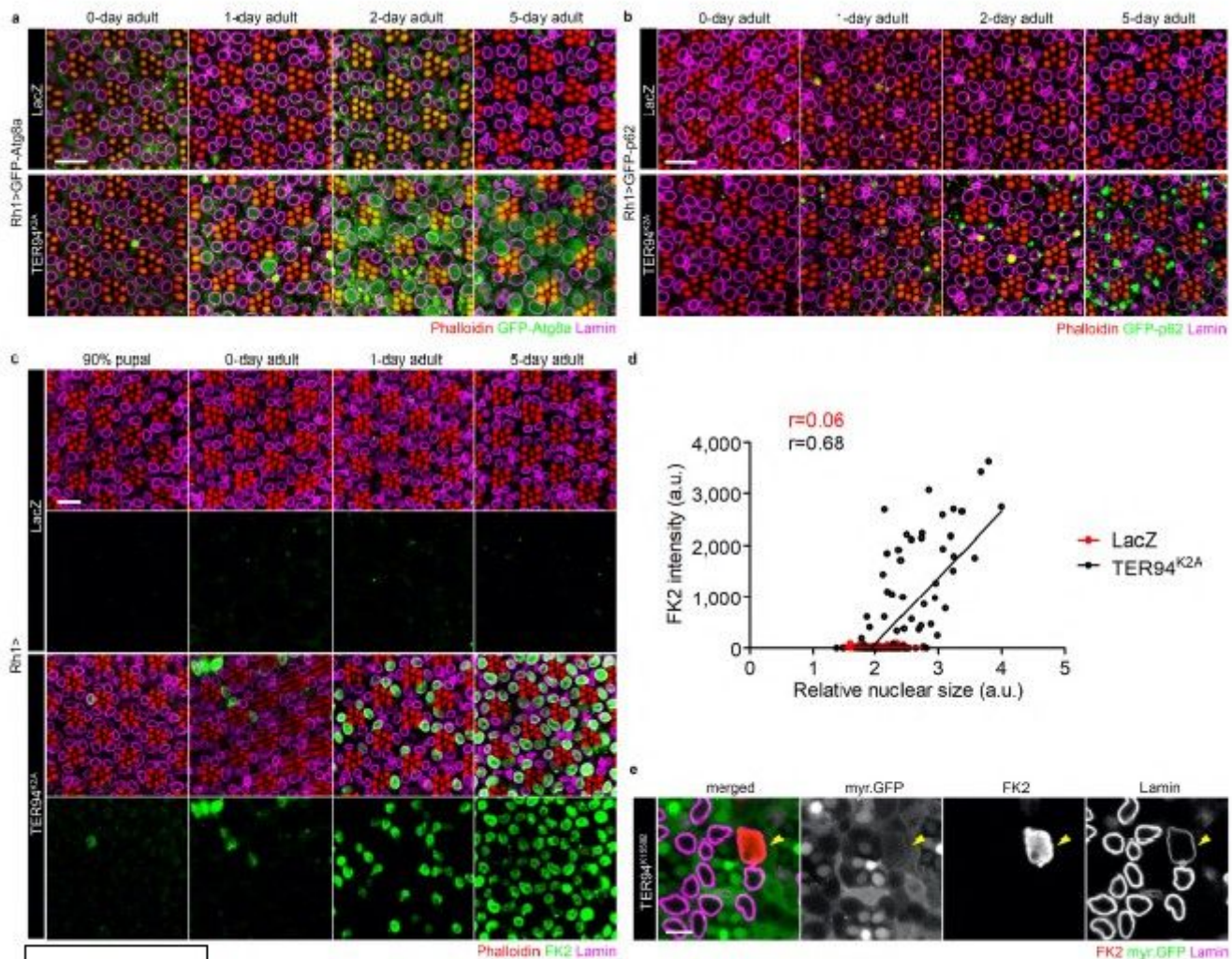


Figure 2

Figure 2

Atg8, p62, and ubiquitinated nuclear proteins accumulate in cells lacking TER94 function. a, b *Drosophila* retinas from freshly-eclosed (0-day) to 5-day-old adults co-expressing GFP-Atg8a with LacZ (control) or TER94K2A (a) or GFP-p62 with LacZ or TER94K2A (b) under the control of Rh1-GAL4 are stained with phalloidin (red) and anti-Lamin (magenta) antibody. c Time-course analysis of the change in nuclear size and the presence of ubiquitinated proteins from late pupal to the 5-day-old adult stage. Pupal or adult eyes expressing LacZ or TER94K2A by Rh1-GAL4 are stained with phalloidin (red), anti-Lamin (magenta), and anti-Ubiquitin conjugates (FK2, green) antibodies. The signals of FK2 staining are separated from the merged images for comparison. d Pearson's correlation analysis of nuclear size and FK2 intensity. Images of 1-day-old adult retina, as shown in panel c, are analyzed. 88-125 nuclei from ≥ 4 independent eyes are measured, and the r values represent Pearson's correlation coefficient in each group. e An adult eye bearing TER94K15502 clone is stained with anti-Lamin (magenta) and anti-Ubiquitin conjugates (FK2, red) antibodies. The absence of myr.GFP marks somatic clone homozygous for TER94K15502 as the arrowhead indicated. The myr.GFP, anti-Lamin, and FK2 signals are shown separately from the merged image and converted to black and white for comparison. Scale bars: 10 μm (a-c), 5 μm (e).

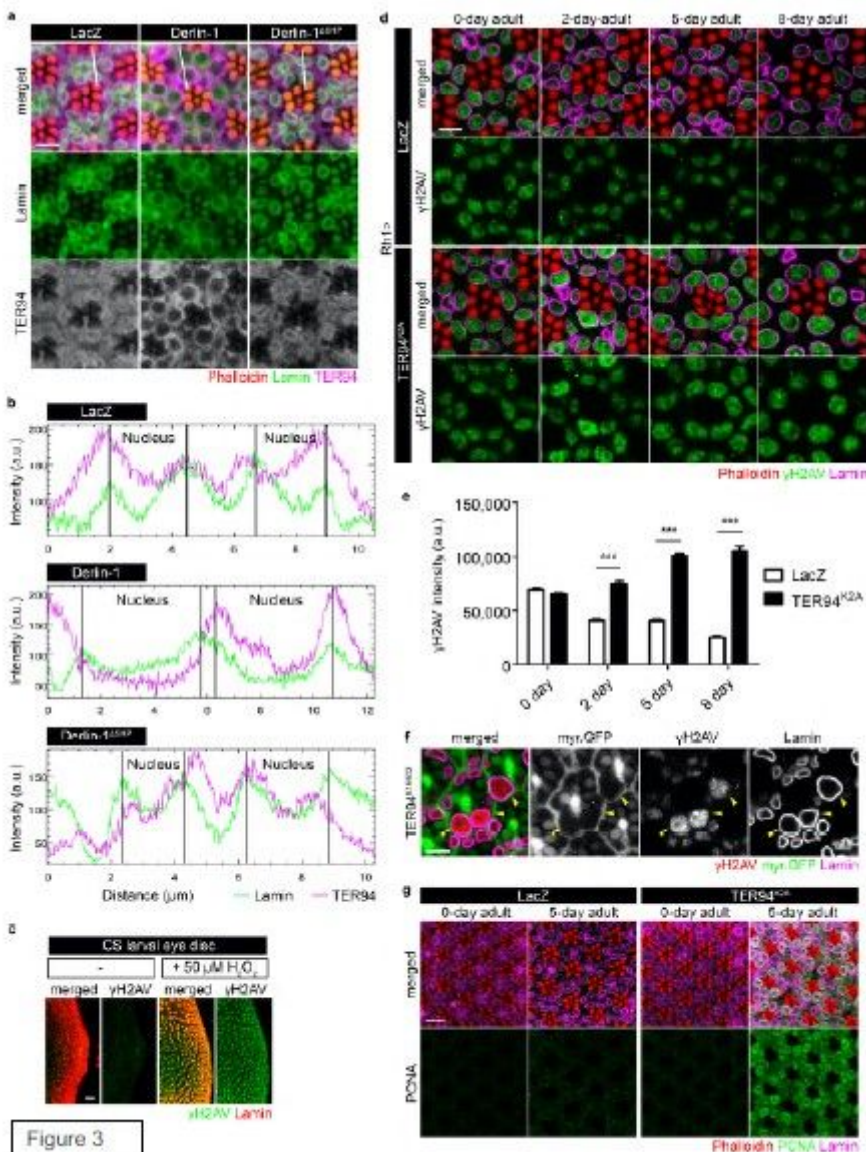


Figure 3

Figure 3

Blocking TER94 function hampers DNA damage repair. a Confocal 844 images of 5- day-old adult retinas expressing indicated transgenes by Rh1-GAL4. The retinas are stained with phalloidin (red), anti-Lamin (green), and anti-TER94 (magenta) antibodies. The anti-Lamin and anti-TER94 signals are shown separately from the merged images for comparison. The anti-TER94 signals are converted to black and white for illustrating the subcellular distribution of TER94. b Analysis of TER94 subcellular distribution. The analyzing range is randomly chosen by drawing a line across two nuclei in each group as the white lines shown in panel (a). Image J measures the intensities of anti-Lamin and anti-TER94 signals along the lines. The peaks of the anti-Lamin signal define the borders of the nuclei. c Confocal images of normal larval eye discs (Canton S; CS) with or without the treatment of DNA damaging agent, 50 μ M H₂O₂. Anti-Lamin (red) and anti- γ H2AV (green) antibodies are used to mark the nuclear envelope and the DNA damage sites. d Time-course analysis of the change in nuclear size and the level of γ H2AV from freshly eclosed (0-day) to 8-day-old adult stage. Adult eyes expressing LacZ (control) or TER94K2A by Rh1-GAL4 are stained with phalloidin (red), anti-Lamin (magenta), and anti- γ H2AV antibodies (green). e Quantification of the anti- γ H2AV signal intensity from flies of indicated genotypes. 56-126 nuclei from ≥ 2 independent eyes are measured in each group. Values shown represent mean \pm SE. *** $p < 0.001$ as compared to Rh1>LacZ of corresponding age (two way ANOVA with Bonferroni post-test). f An adult eye bearing TER94K15502 clone is stained with anti-Lamin (magenta) and anti- γ H2AV (red) antibodies. The absence of myr.GFP marks somatic clone homozygous for TER94K15502 as the yellow arrowheads indicated. The myr.GFP, anti- Lamin, and anti- γ H2AV signals are shown separately from the merged image and converted to black and white for comparison. g Confocal images of adult retinas from flies of the indicated ages expressing LacZ or TER94K2A by Rh1-GAL4 stained with phalloidin (red), anti-Lamin (magenta), and anti-PCNA (green) antibodies. Scale bars: 5 μ m (a, d, f), 20 μ m (c), 10 μ m (g).

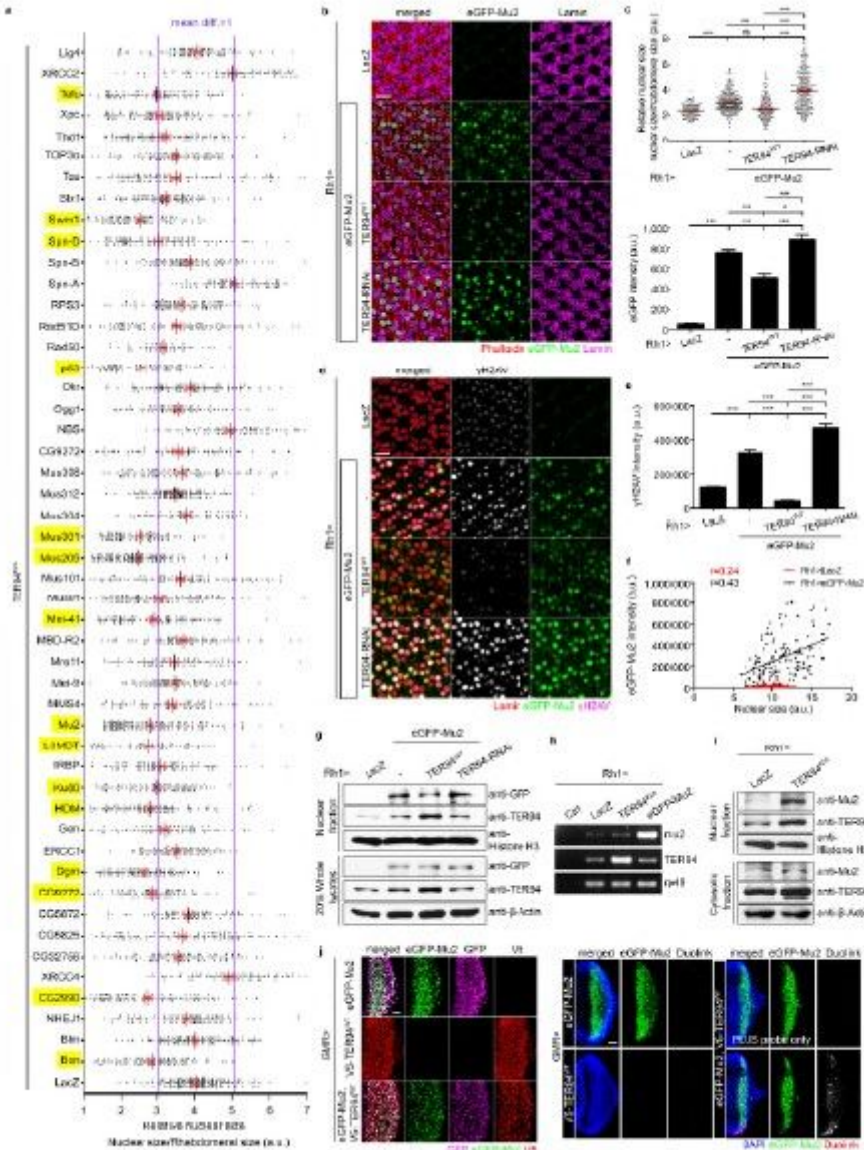


Figure 4

Figure 4

TER94 influences Mu2 level in regulating nuclear size. **a** Quantification of the R1- R6 nuclear area from flies of indicated genotypes. 56-212 nuclei from ≥ 2 independent eyes are measured in each group. The purple lines indicate the difference of the mean equals 1 (mean diff. = 1) as compared to the control (*Rh1>TER94K2A, LacZ*). The DDR genes with mean diff. ≥ 1 are marked in yellow. **b** Confocal images of 7-day-old adult retinas from flies expressing indicated transgenes under the control of Rh1-GAL4 stained with phalloidin (red) and anti-Lamin 877 (magenta) antibody. **c** Quantification of the R1-R6 nuclear area (upper panel, 126-277 nuclei are measured in each group) or eGFP intensity (lower panel, 95-267 nuclei from ≥ 4 independent eyes are measured in each group). **d** Confocal images of 7-day-old adult retinas from flies expressing indicated transgenes under the control of Rh1-GAL4 stained with anti-Lamin (red) and anti- γ H2AV (magenta) antibodies. **e** Quantification of the anti- γ H2AV intensity. 114-268 nuclei from ≥ 3

independent eyes are measured in each group. f Pearson's 883 correlation analysis of nuclear size and eGFP-Mu2 intensity. 134-150 nuclei from ≥ 3 884 independent eyes are measured, and the r values represent Pearson's correlation coefficient in 885 each group. g Western analysis of eGFP-Mu2 level (detected by anti-GFP antibody) in TER94 886 overexpression (TER94WT) or knockdown (TER94-RNAi) backgrounds. The anti-Histone H3 and 887 the anti- β -Actin serve as loading controls for the nuclear and the whole protein lysates. h RT888 PCR measurement of the transcriptional level of mu2 and TER94 from flies expressing indicated genotypes. The control (Ctrl) groups contain all the PCR reaction reagents except the cDNA templates. The level of rp49 serves as an internal control. i Western analysis of endogenous Mu2 level in tissues expressing LacZ (control) or TER94K2A. The detection of anti-Histone H3 and anti- β -Actin serve as loading controls for the nuclear and the cytosolic protein lysates. j Larval eye discs from flies expressing indicated transgenes under the control of GMR-GAL4 are stained with anti-GFP (magenta) and anti-V5 (red) antibodies (left panel). Larvae bearing the same genotypes are subjected to in situ PLA using anti-GFP and anti-V5 antibodies (right panel). The duolink signal reveals proteins in the same complex. The lines in dot plots from a, c represent mean (black) \pm SE (red). The bar charts from c, e represent mean \pm SE. ns, not significant, * $p < 0.05$, *** $p < 0.001$ as compared with indicated genotypes (one-way ANOVA with Bonferroni's multiple comparison test). Scale bars: 10 μm (b, d), 20 μm (j).

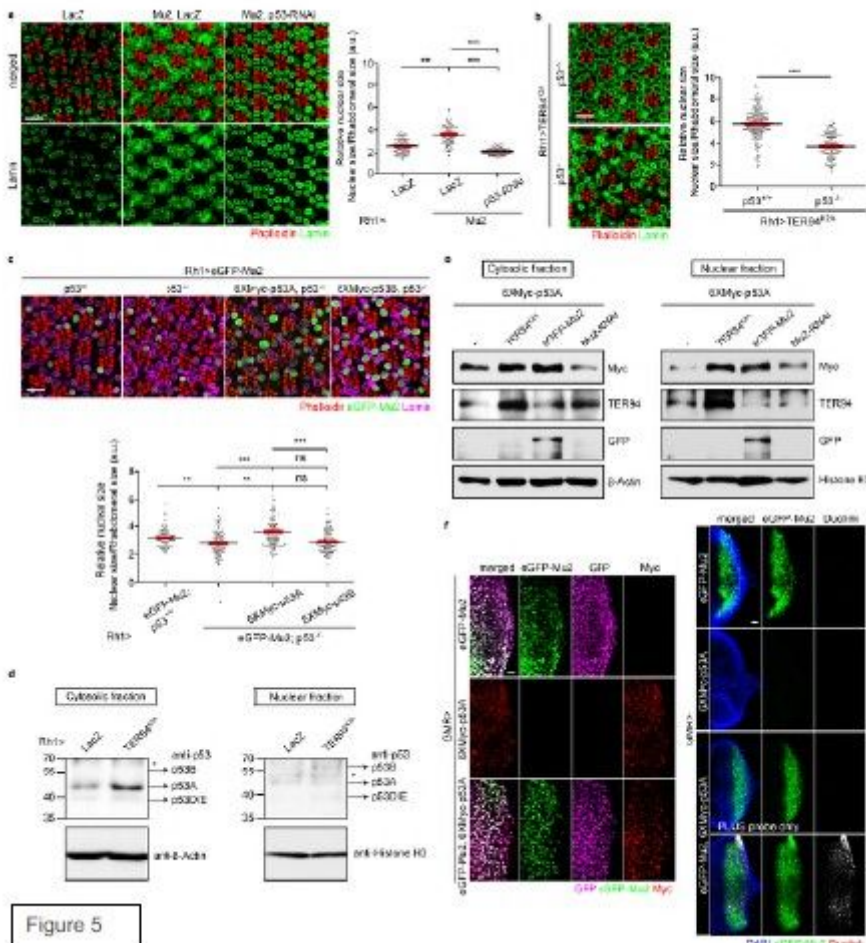


Figure 5

Figure 5

p53 acts downstream of Mu2 in TER94 dysfunction-induced nuclear expansion. a Confocal micrographs of 5-day-old control (Rh1>LacZ) or Rh1>Mu2 adult retina co-expressing LacZ or p53-RNAi stained with phalloidin (red) and anti-Lamin (magenta) antibody (left panel). Quantification of R1-R6 nuclear area from 80-110 nuclei (≥ 3 independent eyes) are measured in each group (right panel). b Confocal images of 6-day-old Rh1>TER94K2A adult retina in wild type (+/+) or p53 null (-/-) background stained with phalloidin (red) and anti-Lamin (green) antibody (left panel). Quantification of R1-R6 nuclear area from 149-219 nuclei (≥ 5 independent eyes) are measured in each group (right panel). c Confocal micrographs of 5-day-old Rh1>Mu2 adult retina in wild type (+/+), p53 null (-/-), 6XMyC-p53A overexpression in p53 null (-/-), and 6XMyC-p53B overexpression in p53 null (-/-) backgrounds stained with phalloidin (red) and anti-Lamin (magenta) antibody (upper panel). Quantification of R1-R6 nuclear area from 80-116 nuclei (≥ 3 independent eyes) are measured in each group (lower panel). The lines in dot plots from a-c represent mean (black) \pm SE (red). ns, not significant, ** $p < 0.01$, *** $p < 0.001$ student's t test, two-tailed (b), one-way ANOVA with Bonferroni's multiple comparison test (a, c). d Western analysis of the cytosolic and the nuclear p53 level in tissues expressing LacZ (control) or TER94K2A under the control of Rh1-GAL4. The arrows indicate distinct p53 isoforms according to their molecular weights and the asterisks mark nonspecific bands. e Larval eye discs expressing indicated genes are stained with anti-GFP (magenta) and anti-Myc (red) antibodies (left panel). Larvae bearing the same genotypes are subjected to in situ PLA using anti-GFP and anti-Myc antibodies (right panel). The duolink signal reveals proteins in the same complex. f Western analysis of the Myc-p53A level in tissues expressing indicated genes. Scale bars: 10 μm (a-c), 20 μm (e).

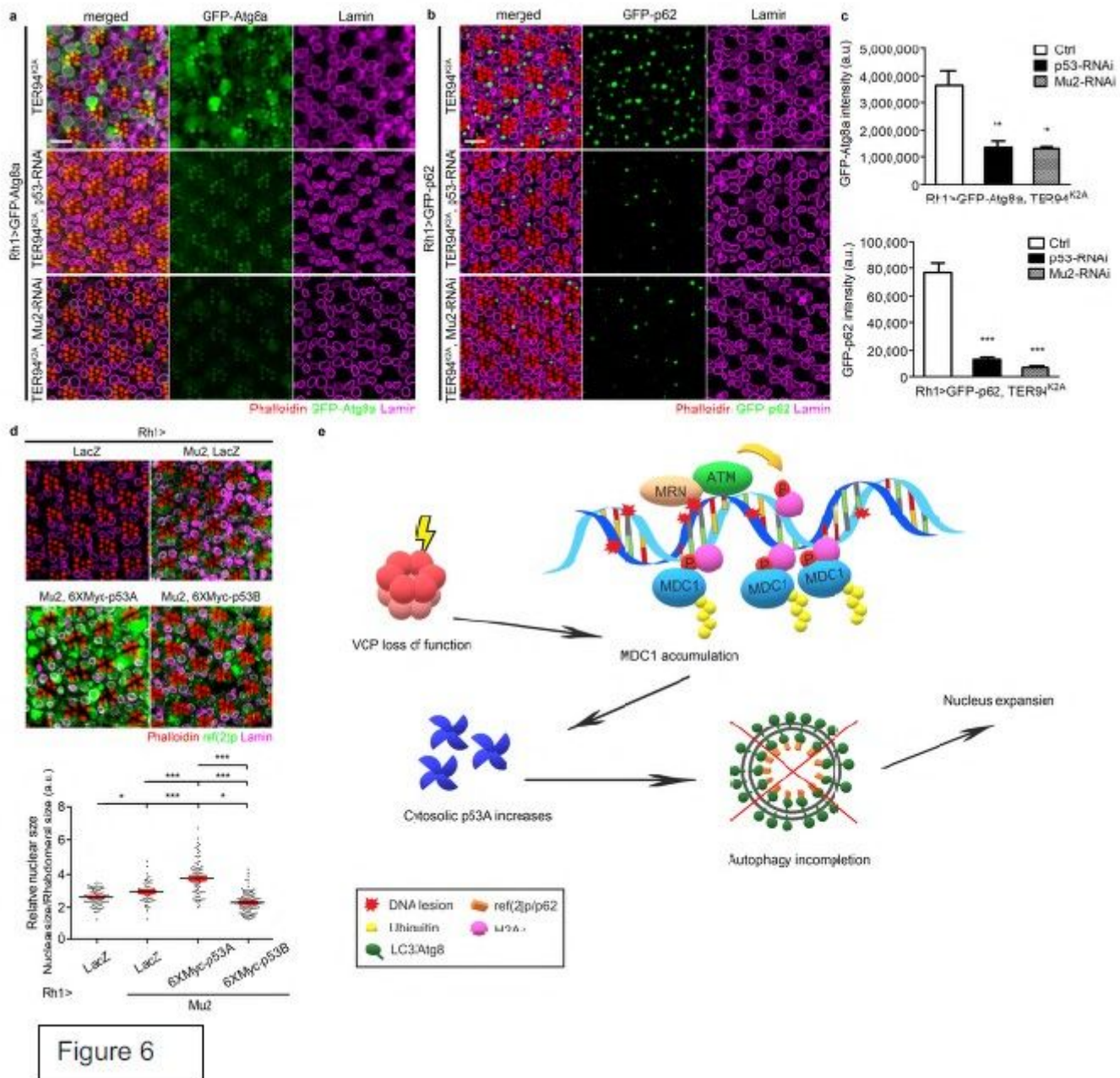


Figure 6

Figure 6

TER94 dysfunction triggers nuclear expansion through p53A-mediated autophagy blockage. a, b Confocal micrographs of 7-day-old Rh1>TER94K2A>GFP-Atg8a (a) or Rh1>TER94K2A>GFP-p62 (b) adult retinas co-expressing p53-RNAi or Mu2-RNAi stained with phalloidin (red) and anti-Lamin (magenta) antibody. c Quantification of the GFP-Atg8a (upper panel) or the GFP-p62 (lower panel) intensity; at least 4 independent eyes are measured in each group. d Confocal micrographs of 5-day-old adult retina expressing LacZ alone (control), co-expressing Mu2 with LacZ or 6XMyc tagged p53 isoforms by Rh1-GAL4 stained with phalloidin (red), anti-Lamin (magenta), and anti-ref(2)p antibodies (upper panel). Quantification of R1-R6 nuclear area from 58-96 nuclei (from ≥ 2 independent eyes) are measured in each group (lower panel). Scale bars: 10 μm (a, b, d). Values represent mean \pm SE. * $p < 0.05$, ** $p < 0.01$, *** $p < 0.001$ (one-way ANOVA with Bonferroni's multiple comparison test) (c, d). e A model for how loss of

VCP function triggers MDC1-p53-mediated autophagy blockage and nuclear expansion. Initially, the MRN complexes recognize DNA lesions and recruit ATM to the damaged sites. The histone variant H2AV near the damaged sites are phosphorylated by ATM, resulting in γ H2AV, which recruits MDC1. Serving as a signaling platform, MDC1 interacts with numerous DNA damage signaling or repairing proteins, including p53. VCP should tightly control the level and the retention period of MDC1 on the injured DNA normally. However, loss of TER94's activity leads to an accumulation of MDC1 and prolongs the interaction between MDC1 and p53, which stabilizes p53, especially p53A. The increased p53A in the cytosol prohibits autophagy flux, which ultimately causes nuclear expansion.

Supplementary Files

This is a list of supplementary files associated with this preprint. Click to download.

- [FigureS1.jpg](#)
- [FigureS2.jpg](#)
- [FigureS3.jpg](#)
- [FigureS4.jpg](#)
- [FigureS5.jpg](#)
- [FigureS6.jpg](#)
- [FigureS7.jpg](#)
- [FigureS8.jpg](#)